UNIVERSITY OF CALIFORNIA SAN DIEGO

2D Image Guided Cell Sorter and 3D Imaging Flow Cytometer

A Dissertation submitted in partial satisfaction of the requirements
for the degree Doctor of Philosophy

in

Electrical Engineering (Medical Devices and Systems)

by

Xinyu Chen

Committee in charge:

Professor Yu-Hwa Lo, Chair
Professor Shaochen Chen
Professor Zhaowei Liu
Professor Tse Nga Ng
Professor Yingxiao Wang

2024

The Dissertation of Xinyu Chen is approved, and it is acceptable in quality and form for publication on microfilm and electronically.

University of California San Diego

2024

DEDICATION

I would like to dedicate my PhD journey to the support and love of my parents. Thank you for allowing me to come to the United States and providing me financial support. To my friends, you have been my pillars of strength, cheering me on through every triumph and comforting me in every setback. Your presence in my life has made this journey not only academically rewarding but also emotionally enriching.

My life in the past six years is not only about academic pursuits, but also a journey of fighting against eating disorders. Severe anorexia and bulimia nervosa used to bring me to the darkest moments when I lost hope for life, again and again. As a result, I would like to express my sincere gratitude to my therapists and dietitians at UC San Diego Student Health Services (SHS), Counseling and Psychological Services (CAPS) and Eating Disorders Center, thank you for your professional consultation and treatment. Without you, I couldn't have made it to where I am right now.

And last but most importantly, I want to thank my beloved boyfriend Haoran, who plays a very essential role in my recovery. Your love and presence are the best medication to my mental illness. I appreciate all the joyful time we spent together and look forward to the future moments that we are going to experience together.

TABLE OF CONTENTS

LIST OF FIGURES

LIST OF TABLES

LIST OF ABBREVIATIONS

FACS	Fluorescent-activated cell sorter
IFC	Imaging flow cytometer
3D	3-dimensional
2D	2-dimensional
PMTs	Photomultiplier tubes
DMs	Dichroic mirrors
PDs	Photodiodes
PCA	Principal component analysis
CV	Coefficient of variance
tSNE	t-stochastic neighbor embedding
FSC	Forward scattering
PDMS	Polydimethylsiloxane
FPGA	Field programmable gate array
PZT	Piezoelectric actuator
CCD	Charge-coupled detector
DNA	Deoxyribonucleic acid
CFSE	Carboxyfluorescein
CNN	Convolutional neural network
DCAEC	Deep convolutional autoencoder
IACS	Intelligent image-activated cell sorter
CPU	Central processing unit
GPU	Graphics processing unit

MACS	Magnetic-activated cell sorting
GUI	Graphical user interface
AOD	Acousto optic deflector
LED	Light emitting diode
HEK	Human Embryonic Kidney
RB	Retinoblastoma
GFP	Green fluorescence protein
AML	Acute myeloid leukemia
COC	Cyclo-olefin copolymer
PSA	Pressure sensitive adhesive
FWHM	Full width half maximum
NB	Needle-shaped beam
DOE	Diffractive optical element
PGMEA	Propylene glycol methyl ether acetate
IPA	Isopropyl alcohol

ACKNOWLEDGEMENTS

Chapter 2, in full, is a reprint of the material as it appears in Applied Physics Letter (APL) Photonics. Chen, Xinyu; Gu, Yi; Chen, Jiajie; Lee Chang-Hung; Gagne, Ivan; Tang, Rui; Waller, Lauren; Zhang, Zunming; Zhang Alex C; Han, Yuanyuan; Wang, Weian; Lian Ian Y; Cho, Sung-Hwan; Lo, Yu-Hwa, AIP Publishing, 2020. The dissertation author was the primary researcher and author of this paper.

Chapter 3, in full, is a reprint of the material as it appears in Applied Physics Letter (APL) Photonics. Chen, Xinyu; Waller, Lauren; Chen, Jiajie; Tang, Rui; Zhang, Zunming; Gagne, Ivan; Gutierrez, Bien; Cho, Sung-Hwan; Tseng, Chi-Yang; Lian Ian Y; Lo, Yu-Hwa, AIP Publishing, 2021. The dissertation author was the primary researcher and author of this paper.

Chapter 4, in part is currently being prepared for submission for publication of the material. Chen, Xinyu; Zhou, Minhong; Zhou, Ziqi; Tang, Rui; Zhang, Zunming; Lo, Yu-Hwa. The dissertation author was the primary researcher and author of this material.

VITA

2018 Bachelor of Science in Optoelectronic Information Science and Engineering, Hefei University of Technology

2020 Master of Science in Electrical Engineering (Medical Devices and Systems), University of California San Diego

2024 Doctor of Philosophy in Electrical Engineering (Medical Devices and Systems), University of California San Diego

FIELD OF STUDY

Major Field: Medical Devices and Systems
Studies in Imaging Flow Cytometer
Professor Yu-Hwa Lo

ABSTRACT OF THE DISSERTATION

2D Image Guided Cell Sorter and 3D Imaging Flow Cytometer

by

Xinyu Chen

Doctor of Philosophy in Electrical Engineering (Medical Devices and Systems)

University of California San Diego, 2024

Professor Yu-Hwa Lo, Chair

Flow cytometry is one of the most used and powerful equipment in cell counting and biomarker detection, and fluorescent-activated cell sorter (FACS) allows users to sort out single cells based on user-defined features. Despite its high throughput, the lack of cell image information may result in false-positive and false-negative, which limits the application of FACS. As a result, imaging flow cytometer (IFC) was developed for imaging of large cell volume in the flow system. However, the integration of sorting function and 3-dimensional (3D)

imaging capabilities in IFC remains to be challenged. Here we developed 2-dimensional (2D) image-guided cell sorters, and 3D imaging flow cytometer, which will be eventually upgraded to a cell sorter based on 3D images. Chapter 2 describes a microfluidic cell sorter that uses fast scanning laser excitation sources and photomultiplier tubes, coupled with real-time image processing, to image and sort cells based on user-defined spatial features. However, flow confinement for most microfluidic devices is generally only one-dimensional using sheath flow. As a result, the equilibrium distribution of cells spreads beyond the focal plane of commonly used Gaussian laser excitation beams, resulting in a large number of blurred images that hinder subsequent cell sorting based on cell image features. To address this issue, chapter 3 presents a Bessel Gaussian beam image-guided cell sorter with an ultra-long depth of focus, enabling focused images of >85% of passing cells.

IFC that can isolate cells of interest in a label-free environment would simplify the process flow, reduce cost, minimize cell disruptions by labeling, and overcome limitations of biomarker availability and specificity. On the other hand, collapsing 3D cell volume to 2D images always greatly reduces information content. To address these needs, we developed a label-free 3D imaging flow cytometer and presented it in chapter 4. The array of photomultiplier tubes (PMTs) collected forward scattering signals from multiple imaging depths, which were reconstructed by software to 3D cell image.

Chapter 1 INTRODUCTION

1 Principles of Flow Cytometry

Flow cytometry is a powerful tool that rapidly analyzes single cells in solution, with a wide range of applications such as immunology, virology, molecular and cancer biology [1]. It analyzes optical and fluorescence characteristics of mixed populations of cells from blood and bone marrow, cells dissociated from solid tissues, human-constructed cell lines and particles such as phytoplankton and nuclei. The obtained data could give valuable information about biochemical, biophysical and molecular aspects of particles [2], including protein expression, apoptosis, cell cycle, and even calcium influx and membrane potential [3].

In a common flow cytometer design, cells or particles are being pumped into a channel with hundreds of micrometers in size, which is called a “flow cell”. Sheath fluid would also be injected into the flow cell at a much higher speed, so the cells would be confined to the center of the channel, passing through one by one. Each cell is illuminated by a single laser, or multiple lasers focusing on the same spot, called the “interrogation zone”. Membrane, nucleus, and organelles make a cell to be a scattering object, which scatters the incident laser light in all directions. On the other hand, cells can also be labeled with viral transfection, immunostaining or staining with fluorescent dyes. These fluorescent compounds absorb light energy, making the electrons rise from ground states to excited states. The excited electrons quickly go back to their ground state while giving the excess energy as photons. The emitted photons are called fluorescence light. People usually choose fluorescent compounds such that each of them will generate fluorescent light that peaks at different colors.

Light signals with mixed wavelengths, generated by laser-particle interaction, are separated by optical elements called dichroic mirrors, followed by band-pass filters. Dichroic mirrors (DMs) spectrally separate light by transmitting and reflecting light as a function of wavelength. For example, long-pass DMs transmit light with a wavelength higher than the cut-off value and reflect light with a wavelength lower than the cut-off value. A band-pass filter allows only a narrow range of wavelengths to pass through, which is close to the emission peak of a fluorescent dye. Behind each band-pass filter is a photodetector, which converts light intensity to electric current. The scattering signals are detected in two directions, forward and side, with the former one generally being considered as indicating cell size and the latter one being considered as indicating cell granularity.

Photodiodes (PDs) and photomultiplier tubes (PMTs) are the two most used detectors in flow cytometry. PMTs amplify the incident photon by secondary electron emission, thus they have higher sensitivity and better performance in detecting weak light signals. However, PDs are much smaller in size and can be easily multiplexed to an array. The current outputs of PMTs or PDs travel to the amplifier, which also serves as a current-to-voltage converter. The analog signals are then sampled by a digitizer for computer processing, and the software displays the scattering or fluorescent intensity of each cell as histograms or plots. Nowadays, with the increased number of excitation lasers and fluorescent channels, large volumes of datasets enable new methods of analysis like principal component analysis (PCA), t-stochastic neighbor embedding (tSNE) to be implemented.

2 Fluorescence Activated Cell Sorter

Classification, detection, and isolation of different cell types among cell populations can bring significant insight to biology and medicine [4-5]. Cell heterogeneity in biological systems

has been a mechanism of maintaining the system's stability and functionality [6]. The cell-to-cell differences in structure, composition, and morphology have demonstrated functional consequences in a variety of biological processes including cell adhesion, immune interactions, intracellular signaling, and cell growth [7-10]. Hence detecting and classifying new cell types in highly heterogeneous biological samples is crucial to understand the complex functions and behaviors of biological systems. On the other hand, in diseased tissues such as cancers, tumor cells display enormous heterogeneity and new types of tumor cells can develop with the progression of the disease. Certain tumor cells, even with very low population, can play significant roles in drug resistance and metastasis [11-12]. All of the above underscore the importance of detecting, classifying, and isolating cell types even for cells of very low abundance. Currently microscopy and FACS are the workhorses to perform such functions, as the former produces high information content, i.e., imaging features of cells, and the latter has the high throughput and the ability of isolating specific cell types based on expression levels of biomarkers.

FACS is an advanced variant of flow cytometry, which can sort a heterogeneous mixture of particles into at least two containers, based on the scattering and/or fluorescence characteristics of each particle. The software allows users to choose their target of interest by defining a numerical or graphical boundary on the one-dimensional or two-dimensional histogram, which is called the gate. Cells whose characteristics fall within the gate will be separated from those cells who do not. A variety of sorting mechanisms have been developed in the past several decades, including electrostatic sorting, microfluidic on-chip sorting, and acoustic sorting.

2.1 Electrostatic Sorting

Electrostatic sorting is the most widely used technique in commercial FACS. An ultrasonic transducer applies vibration to the flow stream, and droplets form at the end of the stream because of rapid pressure fluctuations superimposed upon the ambient pressure [13]. Cells are illuminated by the laser in the flow stream. If the detected signals fall within the gating criteria, a charging pulse, in the order of tens volts, is applied to an electrode which contacts the electrically conducting fluid. The cell-containing droplet will carry charge when it breaks off from the stream. All the droplets, both charged and uncharged, then pass through a 2000V transverse electrostatic field established by two parallel plates. Charged droplets are deflected transversely by an amount proportional to their charge, and the uncharged droplets remain traveling straight down, thus they can be separated to different collection tubes [14].

2.2 Microfluidic Cell Sorting

However, most FACS based on electrostatic sorting are bulky, expensive and require highly skilled personnel to operate, which limits lots of researchers from accessing FACS. As a result, people came up with the idea of applying microfluidic techniques to flow cytometers, and developed cell sorting devices called μFACS. Microfluidics is a research area in which fluids are manipulated on the microscale level. At this scale, people can take advantage of the scaling of many physical laws such as rapid diffusion, laminar flows, Dean flows etc. [15]. Taking the cytometer to a microfluidic platform could transform the device into a compact and low-cost machine. Additionally, microfluidic cartridges are disposable, which means cross-contamination and clogging will not be a concern [16]. Instead of spending countless hours and money on troubleshooting, problems can be solved by simply replacing the cartridge. The three major components of a FACS system: (1) fluidic system, (2) optics system, (3) sorting system, can all be miniaturized in μFACS, while maintaining performance. Here I will look at some of the

recent advancements in microfluidic devices, as well as on-chip high throughput sorting methods.

2.2.1. Microfluidic Hydrodynamic Focusing

Flow focusing has always been an important concern in microfluidic-based flow cytometers. When fluid moves freely in a pipe, due to surface friction, the portions that are close to the walls travel much slower than the portion near the center. The flow velocity profile thus follows a parabolic distribution [17]. The one-dimensional flow focusing on the lateral direction can be easily achieved by adding two flanking sheath flow lines to the center sample flow line. The sheath versus sample flow rate is usually 10:1 [18]. However, particles will still randomly distribute in the channel in the vertical direction. Inconsistent traveling speed of the sample would cause variations in signal intensity, which limits the stability of the instrument.

A significant amount of work has been devoted to developing microfluidic devices with two-dimensional flow focusing. Chiu *et.al.* designed a device where the two sheath channels are 100μm high while the sample channel height is 30μm [19]. The centers of the sample and sheath channel are on the same level, and the tight flow focusing was achieved after they merged in the main channel. The flow properties are visualized by using fluorescent dye mixed in the sample flow. The sample flow was confined to a stream of ~30μm in both directions at 1:40 sample/sheath flow ratio. In beads and cells tests, the coefficient of variance (CV) of the particle velocity was reduced by 50%-87.5%, depending on the sample/sheath flow ratio, compared to the device with 1D flow focusing. However, the multi-layer 3D structure of this device makes the fabrication process very complicated. To solve this problem, Zhao et.al. developed a single layer device with similar performances [20]. The device has four sheath flow inlets, with two of them confine the sample flow in horizontal direction and the other two confine the sample flow

in vertical direction. The key is to add sheath flow number 3 and 4 before and after the sample inlet to squeeze the sample stream. They used rhodamine solution as sample flow and observed that it was confined to an area of about 15μm x 17μm. In the polystyrene beads test, the CV of forward scattering (FSC) intensity is about 7.56%, which is comparable to the traditional flow cytometer using the non-microscale fluidic system.

2.2.2. Microfluidic Cell Sorter with Integrated Piezoelectric Actuator

Numerous types of μFACS have been developed for particle and cell sorting. The most used working principles are electroosmotic [21], dielectrophoretic [22], magnetic [23] and hydrodynamic [24]. However, they all suffer from some limitations like high operation voltage, complicated device fabrication or sample preparation, low throughput, etc. Chen and Cho *et.al.* was able to develop a microfluidic cell sorter based on the mechanical bending of a piezoelectric actuator (PZT) [25-26]. Some key features of this cell sorter are high throughput, low voltage and power and precise control of each single cell. The device, made of polydimethylsiloxane (PDMS), has a 200μm wide main channel, followed by a sorting junction and three sorting channels. The center channel is for collecting unwanted cells and the left and the right channels are for collecting the targeted cells.

The fluorescent or scattering light emitted by the beads or cells was collected by a PMT. The output signal from the PMT was imported into the electronic control system for real-time processing. The control system is programmed with an external driver that has an embedded field programmable gate array (FPGA) chip. If the signal, after denoising, is higher than the user-defined threshold value, it means the particle is the one targeted for sorting. In that case, a pre-defined voltage signal is delivered to the PZT actuator at an appropriate time delay. The PZT actuator, located in the sorting chamber, has a lead-zirconate-titanate (PZT)-stainless steel

bimorphous structure, and it bends upward or downward according to the polarity of the applied voltage. The exact volume of fluid displacement by the PZT actuator can be precisely controlled by the amplitude of the applied voltage. The bending of the PZT actuator induces a transverse displacement of fluid in less than 0.1ms, thus the trajectory of the target cell would change from moving to the center channel to moving to the left or right sorting channel. This sorting device, as well as all the optics and electronics systems, have been commercialized as a product [27].

2.2.3. Microfluidic Cell Sorter with Laser-Induced Jet Sorting

Even though the μFACS in the previous section has been optimized to achieve about 1000 cells per second sorting rate, it is still much lower than the commercial aerosol based FACS, which has a throughput of 70,000 cells per second and 90% purity. As a result, Chen *et.al.* successfully used the phenomena of the pulsed laser induced cavitation bubble to switch particles/cells in high speed [28]. The microfluidic chip made of PDMS consists of a main channel with two outlets, collection and waste. The pulsed channel was in parallel with the main channel and was connected to the main channel through a straight narrow nozzle at the tip of the junction. Allura Red dye was added in the pulsed channel flow. A Q-switched Nd:YVO_4 laser operating at 532nm wavelength was focused through a 100X objective lens into the pulsed channel, which induced an explosive cavitation bubble which expanded and displaced the surrounding fluid. The liquid jet deflected the desired object into the collection channel. FPGA logic was programmed using LabView to perform real-time detection, threshold comparisons, and timed triggering of the pulsed laser. A collection purity of 90% was achieved under a sorting throughput of 3000 particles per second. To further enhance the sorting throughput, later they combined 2D flow focusing microfluidic devices with laser induced jet sorting, and they were able to achieve 90% sorting purity at a speed of 23,000 cells per second [29]. The first version of the device took advantage of a 3D multilayer structure, and the second version was greatly simplified by a non-sheath flow design [30].

3 Imaging flow cytometer (IFC)

In contrast to conventional flow cytometry, which measures forward scattered light to estimate the relative cell size, microscopy, a technology invented in the seventeenth century, yields the exact cell size through its bright field image. While the microscopy system produces rich information from the cell's spatial characteristics, the FACS system used to isolate cells cannot take advantage of such information contents, thus greatly limiting our ability of discovering new, especially rare, cell types the biomarkers of which are not known or sufficiently specific. To address this challenge, imaging flow cytometers, capable of capturing single cell images like a fluorescence microscope while retaining the high throughput of flow cytometer, have been demonstrated. As an integration of fluorescence microscopy and conventional flow cytometry, IFC combines flow cytometry's single-cell identification and high throughput with microscopy's cell image acquisition. Therefore, it becomes an ideal approach to simultaneously fulfill both analysis of morphological characteristics and phenotypic characterization of single cells within an enormous and heterogeneous population [33].

3.1. 2D Imaging Flow Cytometer

3.1.1. Camera-Based IFC

Amnis ImageStream system is the first commercial IFC [34]. Similar to FACS, cells are hydrodynamically focused into a core stream and orthogonally illuminated for both side scattering and fluorescence imaging. Light is collected from the cells with an imaging objective lens, and then passes through a spectral decomposition optical system that directs different spectral bands to different lateral positions. The separated light beams are then projected on a charge-coupled detector (CCD). The CCD is operated using a technique called time-delay-integration (TDI), a specialized detector readout mode that preserves sensitivity and image

quality even with fast relative movement between the detector and the objects being imaged. The sensor arrays on CCD are divided into N columns to detect emission or scattered light of N different spectral ranges from cells. Since its first demonstration, the system has been used to study apoptosis quantification, nuclear translocation, protein co-localization, cell morphological analysis, cell cycle classification, DNA damage, etc. [35-39]. However, The TDI reading out technique requires translation of the cell to be exactly synchronized with the vertical charge transfer of each pixel on the CCD. This means the fluidic system needs to be delicately controlled to avoid inconstant cell speed. Besides, the intrinsic data downloading method of CCD also prevents the system to reach throughput higher than 3000 cells per second [33].

3.1.2. PMT-Based IFC

Compared to CCD, PMT has better sensitivity and dynamic range, as well as lower dark noise. However, the readout of single-pixel PMT is only the number of photons detected in the time domain without spatial information. several systems have been developed to transfer spatial information to either the frequency domain or time domain in order to image the cells in flow system, including serial time-encoded amplified microscopy (STEAM) [40-41], radiofrequency-tagged emission (FIRE) [42], and spatial–temporal transformation [10,43]. STEAM can produce bright field and phase contrast cell images, but not fluorescence images. FIRE has a throughput of up to 50,000 cells per second, but a Fourier transform is required in restoring cell images from the PMT detected waveforms. To solve these problems, Han *et. al.* retrofit a conventional flow cytometer into an IFC system with minimal modification using the spatial–temporal transformation technique. The fluorescence and scattering light emitted from the cells are collected by an objective lens. A spatial filter with an array of slits is inserted at the image plane of the objective lens. Fluorescence, scattering, as well as the transmitted laser light from different

parts of the cell would pass through different slits at different times. The cell images can be reconstructed from the PMT detected waveforms using a simple algorithm. Due to the quick response time of the PMTs, this technique is well suited for high-throughput, real-time image-based cell classification and sorting.

3.2. 3D Imaging Flow Cytometer

The advancement of confocal and light sheet microscopy has made the acquisition of 3D tomography of single cell or even thick tissue accessible. However, only a few groups have been able to demonstrate IFCs with 3D imaging capability [44-48]. In a previous work of our group, a light-sheet scanning illumination design is combined with the spatial-temporal transformation technique, illustrated in the former section, to produce 3D fluorescence and side scattering cell images with a decent throughput of 500 cells per second [49].

The optical interrogation area is defined by a scanning light sheet (x-y plane) of 200-400 μm in height, scanning along the z-direction at 200kHz. A pinhole array on the spatial filter is aligned at a tilting angle to the flow stream, such that each pinhole allows light from voxels with a distinct x index to reach the PMT detector. As the cell flows through pinhole 1, the entire 2D slice of one y-z plane would be excited by the scanning laser. And when the cell flows through the last pinhole the entire cell volume can be imaged. As a result, the resolution in the z-direction is determined by the number of pinholes. The authors were able to image cells labeled by carboxyfluorescein dye (CFSE) and bonded with 1 μm fluorescent carboxylate-modified polystyrene beads, as well as radiation-induced DNA-damaged CMK3 cells. This 3D-IFC system offers unique capabilities for studies of many important biomedical characteristics, such as protein or receptor translocations, tracking of organelle formation or trafficking, chromosome structural aberrations and 3D orientation and polarity. The label-free 3D side scattering images

and 2D transmission images were also proved to carry rich information about the properties and functions of cells because researchers were able to demonstrate cell classification using convolutional neural network (CNN) and deep convolutional autoencoder (DCAEC) based on these images [50-51].

4 Image-guided Cell sorter

4.1 Fluorescence Image-guided Cell Sorter

To better understand the differences that exist between cells, even those with identical , genomes, new approaches are needed to rapidly search through and sort out cells with unique chemical and morphological features from large heterogeneous populations [52]. Imaged guided cell sorting will accelerate a variety of research areas like gene editing, immunotherapy, cell therapy, phenotype drug discovery [53-56]. So far only a few cell sorting systems can isolate cells in this manner, including a real-time image-guided cell sorter using spatial-temporal transformation for cell imaging and machine learning for cell classification [57], and an intelligent image-activated cell sorter (IACS) which can make cell sorting decisions based on a deep CNN [58].

The intelligent IACS has a two-step 2D on-chip hydrodynamic cell focuser to confine the cells in the center of the flow channel. A 3D on-chip acoustic cell focuser is also adopted for maintaining the focused cell stream for a long distance greater than 3cm. The cells are imaged by a frequency-division-multiplexed (FDM) microscope, which scans a linear array of multiple intensity-modulated excitation beams on the cells. The fluorescence and scattering signals are detected by avalanche photodetectors. The cell travelling speed is measured by a speed meter for predicting their arrival time at the sorting position. All the information is fed into a real-time intelligent image processor composed of a FPGA, three central processing units (CPUs), and a

graphics processing unit (GPU). This FPGA-CPU-GPU infrastructure is on a 10-Gbps all-IP network, which enables real-time multidimensional feature extraction, classification, and sort-decision-making. If a sorting decision is made, piezoelectrically actuated dual glass-membrane pumps will isolate the target cells to the sorting channel.

Gu *et.al.* developed another IACS by combining the IFC in [43], the microfluidic cell sorter in [25-26], and machine learning. Cell images are reconstructed using the spatial-temporal transformation algorithm. To better assist users to make sorting decisions, training samples are first flown through the system to produce a set of training data. Off-line processing is employed to construct high resolution cell images. The real-time processing module reconstructs cell images, extracts image features, and makes sorting decisions based on the off-line trained sorting criteria. They were able to sort cells by spatial distribution of specific protein, and number particle binding on cell membrane, as well as radiation-damaged cells, and the classification accuracy was greater than 90%.

To further enhance the image quality, sorting purity and throughput, we came up with a new optics design for the fluorescence image-guided cell sorter, which will be discussed in chapter 2.

4.2 Label-Free Image-guided Cell Sorter

Characterization, classification, and isolation of cell types among a heterogenous population based on their stain-free morphological characteristics can yield significant biological insight, especially when coupled with phenotype-genotype correlations. Cell classification processes often require both the multiparametric spatial information of intracellular structures and high data volume analysis. In recent years, genome sequencing and population genomic analysis have had a profound impact in biological research by enabling high-volume comparative analysis,

enabling new cell type discovery, and uncovering previously unknown cellular heterogeneities [59]. This has significantly increased the need for methods capable of isolating cells of interest in a label-free environment to simplify the process flow, reduce cost, minimize cell disruptions by labeling, and overcome limitations of biomarker availability and specificity. Conventional methods of cell sorting include optical microscopy [60], deterministic lateral displacement [61], density gradient methods [62], and magnetic-activated cell sorting (MACS) [63]. However, these techniques suffer from some of the following aspects, including lack of specificity, low throughput, high cell loss, population-based sorting without single cell resolution, and the need for biochemical labeling.

Image-guided cell sorters have greatly pushed the field of label-free cell sorting forward. This microfluidic-based technology enables the highly informative morphological and spatial characterization of intracellular structures and subsequent sorting of cells of interest at a throughput of over two hundred cells per second [64]. Various possible configurations exist, each with unique characteristics and applications ranging from inexpensive, custom laboratory tools to precise clinical instruments. Examples of compatible on-chip cell sorting techniques include surface acoustic waves (SAWs) [65], magnetic forces [66], and dielectrophoretic forces [67]. An image guided cell sorter based on 2D transmission images will be presented in Chapter 3. A newly developed image guided cell sorter based on 3D forward scattering images will be presented in Chapter 4.

Chapter 2 IMAGE GUIDED CELL SORTER USING FAST SCANNING LASER

1. Materials and Methods

1.1 Overall System Design of Image-Guided Cell sorter

The overall system architecture is shown in Figure 2.1(a). The optical system interrogates each travelling cell in the microfluidic channel by scanning laser excitation beams and generates temporal fluorescent and transmission signal waveforms of each cell. These optical signals, after being detected by PMTs and converted to electronic waveforms, are sent to a FPGA that reconstructs the cell image from these waveforms in real time. The image features are then extracted and compared against the cell sorting criteria, or the "sorting gate", to determine if the cell falls within the gated region. If so, then the FPGA sends a voltage signal to activate the on-chip piezoelectric actuator. Here we choose on-chip PZT actuation due to its low-cost and manufacturability, suitable for disposable devices to prevent cross contamination [25-26]. Under the applied voltage signal, the piezoelectric actuator bends upward or downward mechanically, deflecting the flow and the target cell within the flow into the designated channel in the mode of population sorting where the selected cells are sorted into a designated collection tube. In the mode of single-cell sorting, each deflected single cell exits the designated channel in a cartridge and enters a programmable cell-placement unit that places each cell into a well in the 386-well plate. The programmable cell placement unit relates the cell in each well to the cell's image features, allowing users to check the cell image, the image features, and its "position" within the "sorting gate" or within one of the "clusters" the cell belongs to.

While the real-time process is carried out by the FPGA, many off-line processes also take place in parallel. The cell images are stored and further processed to help users to visually inspect the cells. Via a graphical user interface (GUI), users can use these images and their feature distribution charts to (re)define or (re)classify cells and modify the gating criteria for cell isolation.

1.2 Design of Imaging System

Within the microfluidic device shown in Figure. 2.1I, suspended cells are hydro-dynamically focused to the center of the channel by a sheath flow. At the optical interrogation zone, each cell is illuminated simultaneously by a scanning dual-wavelength 488/561 nm laser for imaging and a non-scanning 455 nm light emitting diode (LED) for cell speed measurement. The 488/561 nm wavelength laser is coupled to an Acousto Optic Deflector (AOD) (OAD948, Isomet) to create a scanning beam along the y-direction (width of the microfluidic channel) with a spot size of 1μm in diameter. Two 10X (NA=0.28) objective lenses (378-803-3, Mitutoyo) on the opposite sides of the microfluidic channel are used, one for focusing the scanning laser illumination beam and the other to collect the fluorescent or transmitted light. Higher than 10X objectives can be used, if preferred, to enhance the resolution and light collection efficiency, with a tradeoff for the depth of focus.

A series of dichroic mirrors with different reflection bands separate LED, transmission, and fluorescent signals to different channels, which are detected by PMTs (H10721-20, Hamamatsu). A spatial mask, having a design of two slits separated in the cell flow (z-) direction, is placed at the image plane of the optical system to generate speed information signal. Depending on the scanning range of AOD and the signal recording time period, the field of view

is chosen to be 30μm by 30μm, which covers the size of most biological cells. The resolution is determined by the diffraction limit of the objective lens, which is 1μm here.

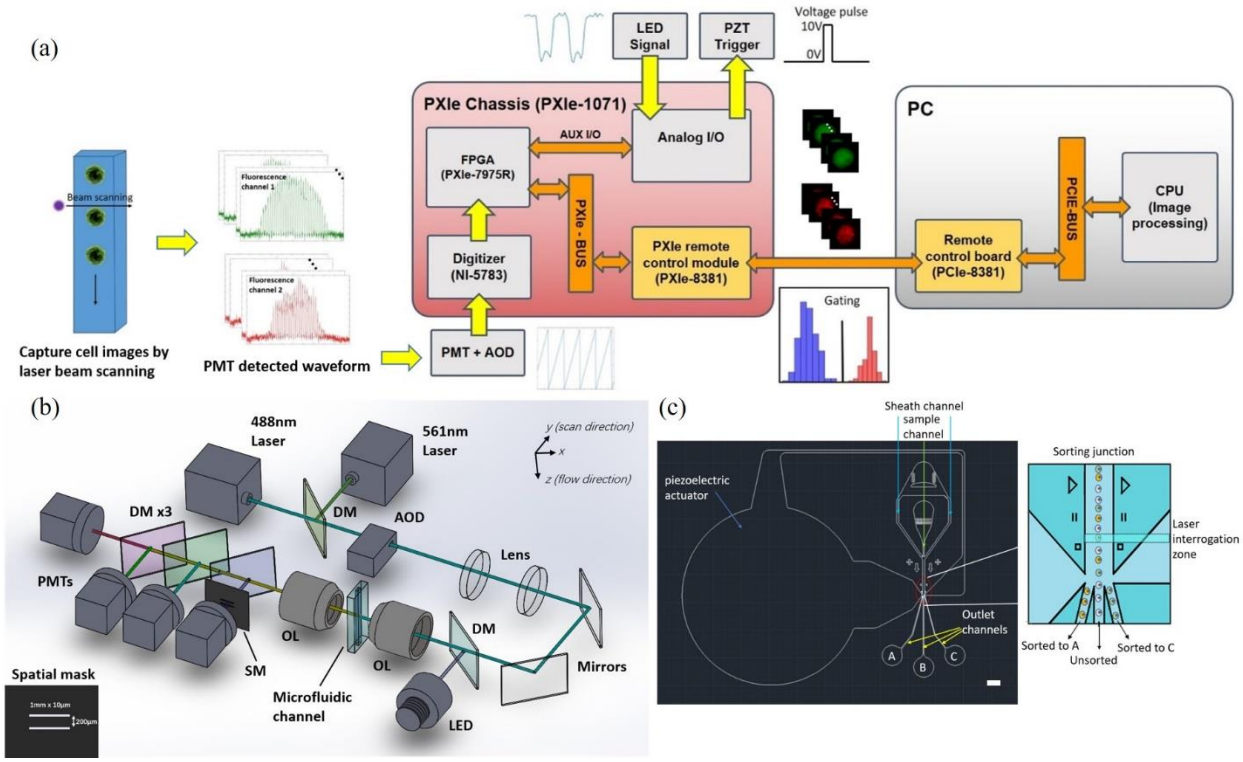

Figure 2.1. (a). Overall system architecture. The scanning laser beam and the cell travel produce an equivalence of a 2D raster scanning system. The bright field and fluorescent signals of the cell are detected by PMTs and the temporal signals are reconstructed to form cell images via real-time processing by a field-programmable-gate-array (FPGA). Meanwhile, the features of each cell image are extracted by a PC or GPU. According to the sorting criteria (gating) based on user-selected image features, the on-chip piezoelectric (PZT) actuator is triggered to sort out cells that have the target features. (b). Design of imaging system. AOD, acousto-optic deflector; DM, dichroic mirror; OL, 10X/0.28 objective lens; PMTs, photomultiplier tubes; SM, the spatial mask for cell speed detection with its design shown on the left. (c). Microfluidic chip design. Suspended cells are focused to the center of the microfluidic channel by a sheath flow. The on-chip piezoelectric actuator bends upward or downward mechanically, deflecting the flow and the target cell within the flow into the designated channel. Scale bar: 1mm.

1.3 Real-time Image processing

To achieve image-guided cell sorting with high throughput, real-time processing and computation of cell image features against the “sorting gate” are required. A FPGA-CPU (or FPGA-GPU) hybrid design is adopted to meet such requirements. The voltage waveform

modulating the AOD and the detected PMT signals from each cell are acquired and digitized. FPGA reconstructs the cell images from the acquired signals based on the principle described next, and the reconstructed cell images are transferred to the CPU for imaging feature extraction. Dozens of image features, which include area, perimeter, shape, circularity, concentricity, aspect ratio (major axis length/minor axis length), integrated intensity, mean intensity (intensity divided by area), standard variation of intensity over space, granularity, spot count, etc. from each fluorescent color and the transmitted signal are extracted, compared, and analyzed in a parallel fashion. Then the features directly related to the cell sorting criteria are transferred back to the FPGA. These image features of each cell passing the interrogation zone is computed in less than 1ms in most cases.

The system contains a user-interface (UI) that can display cell images, histograms of chosen cell features, and 2D distribution plots. Users can go through these histograms or plots to decide by themselves or rely on the built-in algorithms to determine which features are most relevant to the intended applications and can be used as the "sorting gate". The process is interactive and intuitive and allows the cell sample to be divided into subpopulations characterized by cell image features (e.g. spatial distribution of the fluorescent intensity, shape or size of cells or organelles). To sort a cell, a voltage pulse is applied to the on-chip piezoelectric PZT actuator, which instantaneously bends the bimorph PZT disk to deflect the cell away from the central flow into the sorting channel.

1.4 Image Reconstruction Principle and Algorithm

1.4.1 Mathematical model of waveform-image transformation

The detected PMT measured signal S(t) is related to the object $O(y, z)$ by the following equation:

$$S(t) = C \iint_{field\ of\ view} O(y,z) \cdot psf(y-y', z-z')dydz \quad (2.1)$$

where C is a proportional constant due to the effect of optical loss and detector quantum efficiency, $O(y,z)$ is the spatial distribution of the object (cell), and $psf(y-y', z-z')$ is the point spread function of illumination light, with (y', z') being the center of the excitation beam.

In the image-guided cell sorter, the object is illuminated by a Gaussian beam, and its electrical field can be written as

$$\mathrm{E(y,z)} = E_0 \frac{W_0}{W(x)} exp[-\frac{y^2+z^2}{W^2(x)}]exp(-jkx + j\varphi) \quad (2.2)$$

where x is the beam propagating direction, $W(x)$ is beam width, k is wave vector.

The depth of focus can be calculated by:

$$2z_0 = \frac{2\pi {W_0}^2}{\lambda} \quad (2.3)$$

where z_0 is the half focal depth and W_0 is the radius of beam waist at the focal spot. Due to the use of 10X objectives for excitation and light detection, the depth of focus is approximately 10μm. Here we ignore the effect of beam waist change and treat cells that are within the depth of focus. Considering the excitation light intensity which the fluorescent signal is proportional to, we can write:

$$psf(y-y', z-z') = k\ exp\left[-\frac{(y-y')^2+(z-z')^2}{2\sigma^2}\right] \quad (2.4)$$

where $\sigma = \frac{1}{2}W_0$. Substitute (2.4) into (2.1) and augment the limits of the double integral from the finite field of view to infinity,

$$S(t) = C \iint_{-\infty}^{\infty} O(y,z) \cdot kexp\left[-\frac{(y-y')^2+(z-z')^2}{2\sigma^2}\right][u(y-y_{min}) - u(y-y_{max})][u(z-$$

$$z_{min}) - u(z-z_{max})]\, dydz = C\ O'(y,z) * exp\left[-\frac{y^2+z^2}{2\sigma^2}\right] \quad (2.5)$$

where $O'(y,z) = O(y,z)[u(y-y_{min}) - u(y-y_{max})][u(z-z_{min}) - u(z-z_{max})]$. u is the Heaviside step function. $y_{min}, y_{max}, z_{min}, z_{max}$ correspond to the limits for the field of view.

Next, we relate the position of the beam center (y', z') to the time, t, when the cell enters the field of view. Since the cell is travelling in the z-direction,

$$z' = v_{z,cell} \cdot t \quad (2.6)$$

Let t^* denote the interval between the time when the cell enters the field of view and the beginning of next laser scanning cycle. We can write:

$$y' = remainder\left(\frac{t+t^*}{1/f}\right) \cdot v_{y,scan} \quad (2.7)$$

where f is AOD scanning frequency; $v_{y,scan}$ is laser beam scanning speed in the y-direction, and $v_{y,scan} = \frac{laser\ scanning\ range}{1/f}$.

Using the relations in Eqs. (2.6 and 2.7), we can represent the measured PMT signal $S(t)$ as $S(y', z')$. The 2D spatial Fourier transform on both sides of Eq. (2.5) becomes:

$$S(f_y, f_z) = C\mathcal{F}(O')\mathcal{F}\left(exp\left[-\frac{y^2+z^2}{2\sigma^2}\right]\right) = D\mathcal{F}(O')exp\left[-\frac{\sigma^2(2\pi)^2(f_y^2+f_z^2)}{2}\right] \quad (2.8)$$

where D includes C and all other coefficients that produce no effect in our process of finding the cell image $O(y,z)$. For convenience, in the following we will omit all such proportional constants and rewrite Eq. (2.8) as

$$\mathcal{F}(O') = S(f_y, f_z)exp\left[\frac{\sigma^2(2\pi)^2(f_y^2+f_z^2)}{2}\right] \quad (2.9)$$

For cells having their entire images within the field of view (i.e. non-truncated cell images), the intensity at the boundary of and outside the field of view can all be set to be zero. This means $O(y,z) = O'(y,z)$, and as a result, $\mathcal{F}[O] = \mathcal{F}[O']$. Under this condition,

$$\mathcal{F}[O] = S(f_y, f_z) exp\left[\frac{\sigma^2(2\pi)^2(f_y^2+f_z^2)}{2}\right] \quad (2.10)$$

Taking the 2D inverse Fourier transform of (2.10), we have:

$$O(y,z) = \iint_{f_y,f_z=-\infty}^{\infty} S(f_y, f_z) exp\left[\frac{\sigma^2(2\pi)^2(f_y^2+f_z^2)}{2}\right] \cdot exp[j2\pi(f_y y + f_z z)] df_y df_z \quad (2.11)$$

From Eq. (2.11), we can construct the cell image, $O(y,z)$, from the spatial Fourier transform, $S(f_y, f_z)$, of the measured PMT signal. This process can, in principle, yield cell images with higher resolution than the spot size of Gaussian beam if the signal has a high S/N ratio. However, the above method can be computationally intensive and is more suitable for off-line processes. For the real-time process, we can reduce the computation complexity considerably by approximating the point spread function of a Gaussian beam by a delta function,

$$psf(y-y', z-z') = A\delta(y-y', z-z') \quad (2.12)$$

Substituting Eq. (2.12) into Eq. (2.1) and using Eqs. (2.6,2.7), we can directly relate the PMT signal to the cell image:

$$S(t) = S(y', z') = \iint_{field\ of\ view} O(y,z) \cdot A\delta(y-y', z-z')\, dydz = A\, O(y', z') \quad (2.13)$$

From Eq. (2.13), at each "t", there exists a corresponding (y', z') within the field of view such that the magnitude $S(t)$ corresponds to the transmission or fluorescent intensity of the cell at position (y', z').

A comparison of images reconstructed from a Gaussian beam using Eq. (2.11) and from a delta function approximation using Eq. (2.13) is shown in Fig. 2.2. We observe that for both bead and cell images, the difference is insignificant. For real-time processing, the delta function approximation offers a convenient approach although the image resolution is limited by the spot size of Gaussian beam. Unless specially mentioned, we use the delta function approximation to process cell images for image-guided sorting in this paper.

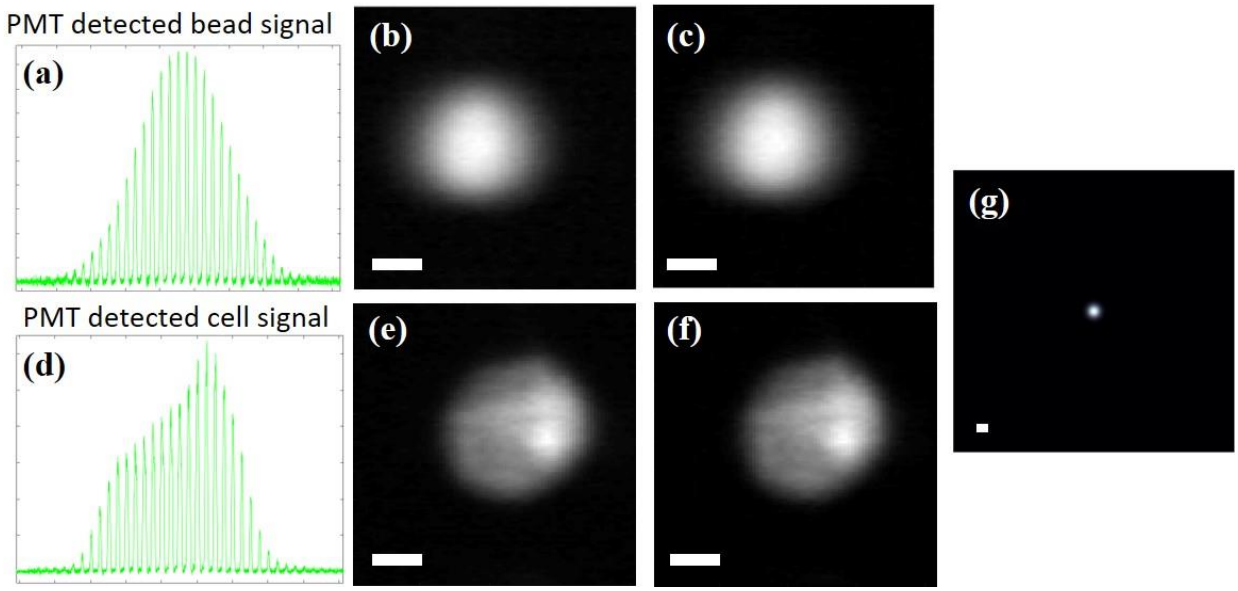

Figure 2.2. (a) Fluorescent signal of a 15μm bead. (b) Reconstructed bead image using delta function approximation. Scale bar: 5μm. (c) Reconstructed bead image using the true Gaussian beam. Scale bar: 5μm. (d) Fluorescent signal of a cell. I Reconstructed cell image using delta function approximation. Scale bar: 5μm. (f) Reconstructed cell image using the true Gaussian beam. Scale bar: 5μm. (g) Simulated PSF of the Gaussian beam within 30x30μm^2 field of view. Scale bar: 1μm.

1.4.2 Digital Implementation of Image Reconstruction Algorithm

In a digital implementation with the "delta function approximate point-spread-function", our image construction process contains the following steps: I. conversion of the temporal waveform of PMT into a 2D cell image, II. Correction of the effect caused by a time delay between the modulating voltage applied to the AOD and the corresponding laser beam spot, which we call correction of "phase shift" below, and III. Correction of image contraction or stretch due to the effect of cell travelling speed, which we call "image resizing" below.

I. Conversion of the temporal waveform of PMT output into a 2D cell image without cell speed correction.

We use a periodic sawtooth waveform to modulate the AOD. Within each period, the AOD scans the laser spot from one extreme position to another at a uniform speed along the

channel width (y-axis), and then the laser spot returns quickly (in ~150ns) to the starting position for the next scan. Each time the AOD scans the laser excitation beam spot in the y direction, the resulting fluorescent or transmission signals recorded by the PMTs are registered to form a 1D slice of the cell image along the y-direction. Since the cell is travelling in the z-direction during laser scanning, the laser y-scanning actually produces a line scan of the cell image with a small angle ($\theta \sim tan^{-1}(\frac{v_{z,cell}}{v_{y,scan}})$). Due to the much faster laser beam scanning speed than the cell travel speed (e.g. 600cm/s for $v_{y,scan}$ and 20cm/s for $v_{z,cell}$), such effect is rather small and can be neglected or easily corrected, if needed. Mathematically, each cell travelling through the optical interrogation area will produce a series of image data registered as $S^{z_1}(y_1),\ S^{z_1}(y_2)\ \dots\ ,\ S^{z_1}(y_N);\ S^{z_2}(y_1), S^{z_2}(y_2)\ \dots\ ,\ S^{z_2}(y_N); \dots S^{z_M}(y_1), S^{z_M}(y_2)\ \dots . S^{z_M}(y_N)$. The above data set can be arranged into a MxN matrix, representing a 2D cell image in the y-z plane. The MxN matrix defines the pixels of the image frame that is 30μmx30μm, in accordance with the physical scanning range of the laser. The column number (N) is determined by the ratio of the A/D sampling rate and AOD scanning frequency, and the row number (M) is determined by the scanning range and cell speed. A higher ratio of the A/D converter sampling rate to the AOD scanning rate and a slower cell traveling speed will yield smaller pixel size and thus higher pixel resolution at the expense of throughput. In our experiment, we have used 25MHz A/D sampling rate, 200KHz AOD scanning rate, and an average cell speed of 20 cm/s, giving rise to an effective pixel size of 1 μm (z-direction) by 0.24μm (y-direction). To construct cell images from the data stream, we first find the troughs and peaks of the voltage waveform that modulates the AOD as they specify the beginning and ending times and the duration of each line scanning cycle. We then stitch each 1D slice of PMT readout, $S^{z_i}(y_1), S^{z_i}(y_2)\ \dots\ ,\ S^{z_i}(y_N)$, to form an MxN matrix, which gives rise to the raw image (Fig 2.3(a)).

II. Correction of the “phase shift”.

Under DC bias condition, the laser beam spot matches the applied voltage to the AOD in a fashion that the laser beam points to the leftmost position at the lowest AOD bias voltage. However, when a sawtooth voltage waveform is applied, a time delay Δt develops between the laser beam spot position and the voltage value due to the electric capacitance of the AOD and the parasitic capacitance. To be discussed next, this time delay can cause a “phase shift” in the cell image. To detect the time delay and the amount of phase shift, we choose a few z- (cell flow) positions and plot the transmitted light intensity along the y- (laser scanning) direction. Due to time delay, the intensity plot along the y-direction may not show a continuous profile but a profile of two discrete regimes (Fig 2.3(b)). By shifting the left part of the profile to join the right part to make a continuous intensity profile and to center the entire intensity profile within the image frame, we can obtain the “phase-shift corrected image”. The same correction for the phase shift is also applicable to the fluorescent signals and other scattering signals since they are all produced by the same scanning laser beam and synchronized with each other.

III. Correction of image distortion caused by cell speed variation

Even with hydrodynamic flow focusing, cells may not be at the same position in the microfluidic channel due to the variation of cell size, stiffness, and other effects. In a laminar flow where cell speed is determined by the cell position within the channel, the above effects can produce appreciable speed variations among cells. As described previously, the process of cell image construction converts a temporary signal (detected by PMTs) into a spatial signal represented by an MxN matrix, and cell speed variation directly affects the value of M, determined by the ratio of the laser scanning speed to the cell travel speed. Under a predefined image frame with 30x30 pixels, the reconstructed cell image would be contracted for cells at

greater than the average speed and elongated for those at lower than the average speed. Therefore, to form the correct cell image, we need to measure the speed of each cell, which is achieved by a static LED light source and a spatial mask described next.

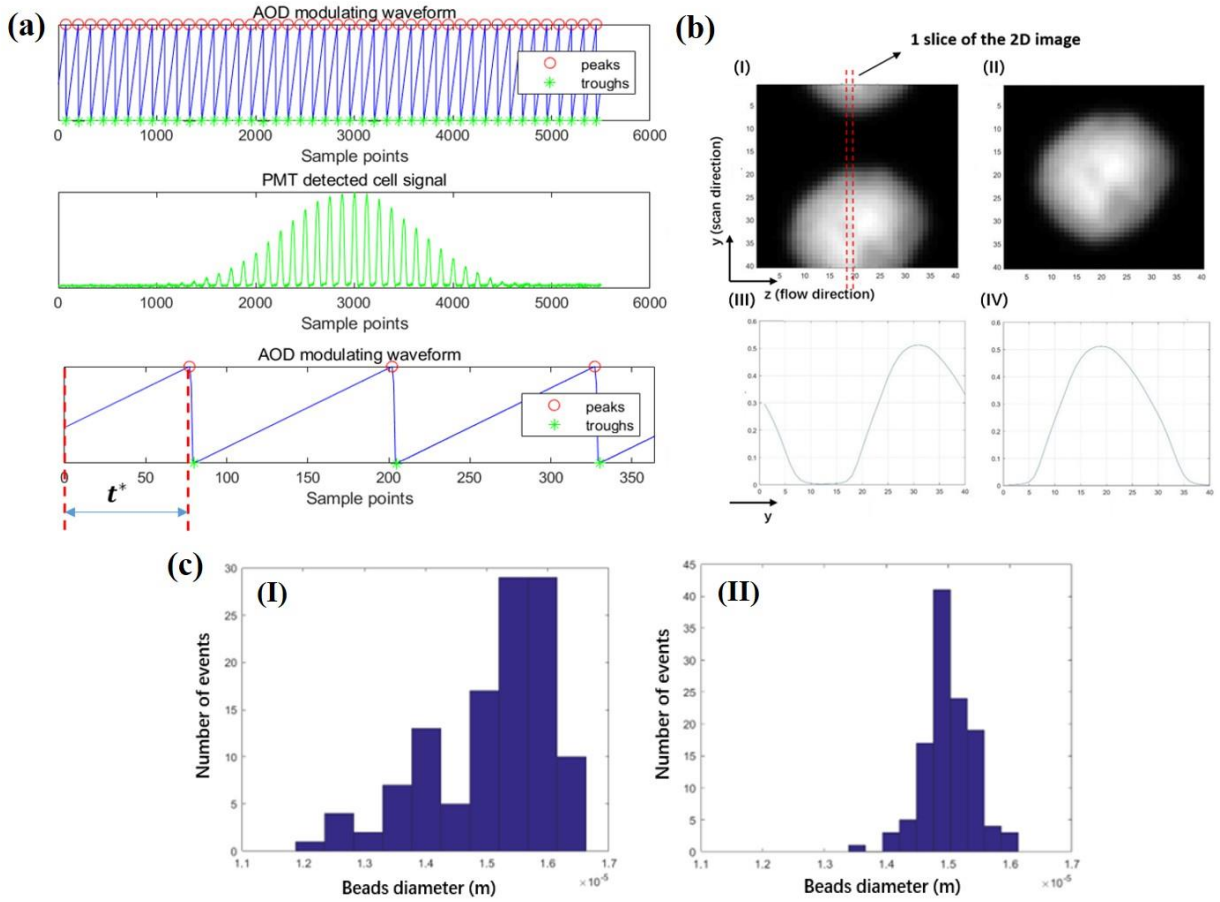

Figure 2.3. Corrections of "phase shift" effect and "cell velocity variation effect" in image reconstruction process. (a) Temporal waveforms of AOD modulating voltage and PMT output. t^* denotes the interval between the time when the cell enters the field of view and the beginning of next laser scanning cycle, which can cause "phase shift" for the reconstructed image. (b) Correction of the time delay, t^*, between the AOD modulating voltage and the corresponding laser beam spot position. (I) reconstructed image before phase shift correction, (II) reconstructed image after phase shift correction, (III) integrated signal along the z-axis before phase shift correction, (IV) integrated signal along the z-axis after phase shift correction. (c) Correction of the cell velocity effect: histograms of measured diameter of 15μm beads before (I) and after (II) speed variation correction.

As shown in Fig 2.1. (b), the LED light passing the sample and the objective lenses is reflected by the first dichroic mirror after the detection objective lens, and transmits through the spatial mask before reaching the PMT. The transmitted LED light through the slit produces a dip

in the light intensity each time a cell travels through the light path due to light scattering or absorption. The two parallel slits on the spatial mask are 10μm wide and 1mm long each, with a center-to-center distance of 200μm. By measuring the time interval between two dips, the travelling speed of each individual cell can be calculated, and the measured cell speed can be used to find the "true image frame" along the cell travel (z-) direction. As a result, image distortion along the z-direction due to cell speed variations can be corrected.

2. Experimental Results

2.1 System calibration

To characterize the performance of the image-guided cell sorter, we first imaged suspended fluorescent (Dragon Green) polystyrene beads with a mean diameter of 0.96μm (Bangs Laboratories, FSDG004). As shown in Fig 2.4(a), the transmission and fluorescent images of these beads allow us to characterize the optical resolution and sensitivity of the system.

To demonstrate image-guided sorting capabilities, we first sort beads by their diameter. The 1:1 mixture of polystyrene beads of two different diameters, 10μm and 15μm, are isolated by the image-guided cell sorter. The example images generated by the system are shown in Fig 2.4(b), and the diameter histogram is shown in Fig 2.4(c). To verify the purity of the sorted sample, the beads that are sorted by their diameter are subsequently imaged by a fluorescent microscope; and the results based on 170 fluorescent microscope images indicate a sorting purity of 97%.

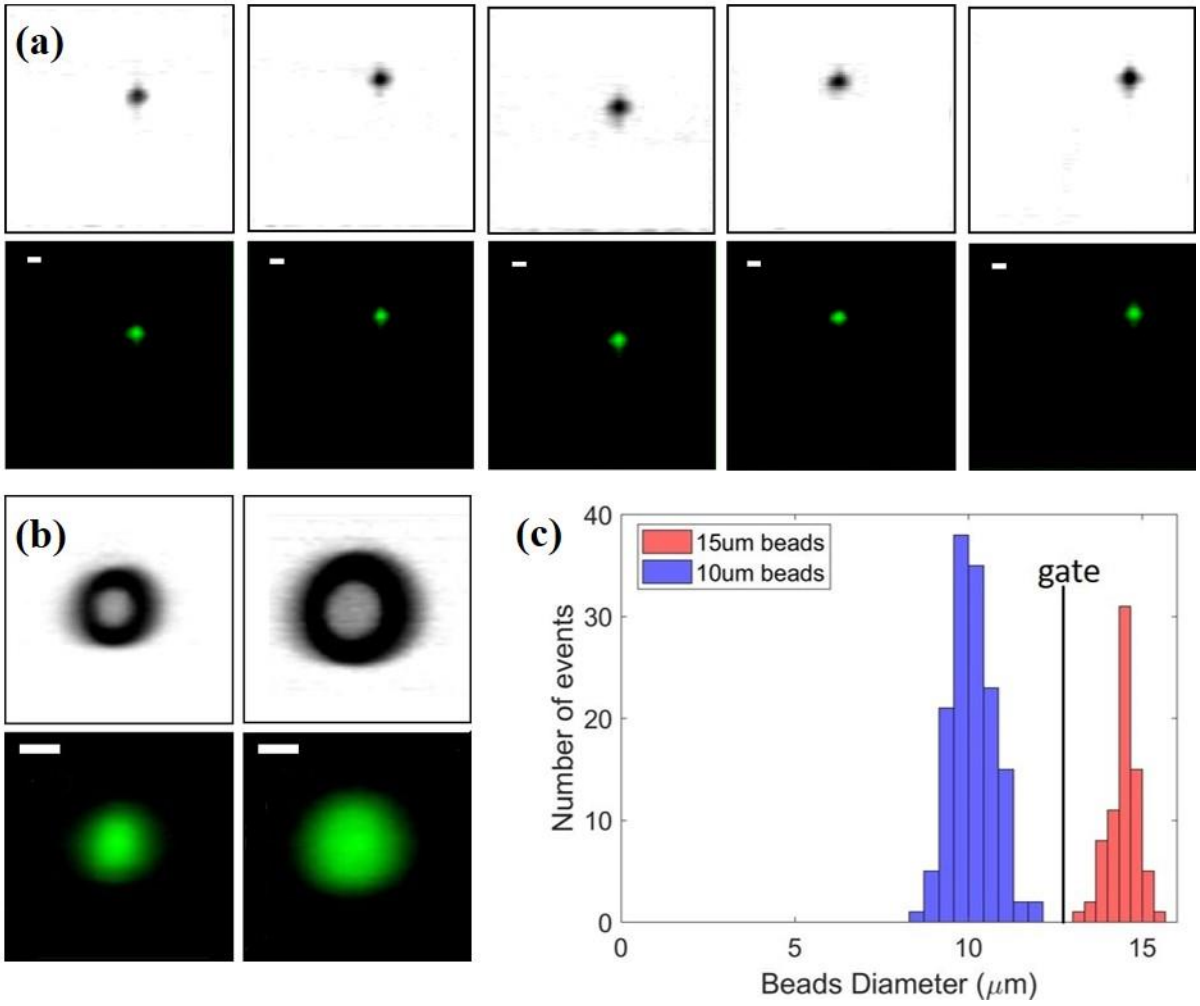

Figure 2.4. Image and histogram of polystyrene beads generated by the image-guided cell sorter. (a) Example transmission images (first row) and fluorescent images (second row) of polystyrene beads with 0.96μm diameter. Scale bar: 2μm (b) Example transmission images (first row) and fluorescent images (second row) of polystyrene beads with 10μm (first column) and 15μm (second column) diameter. Scale bar: 5μm. (c) Histogram of bead diameter.

2.2 Sorting of Cells According to the Number of Bonded Beads

Specific cell-surface markers on immune cells or stem cells indicate their unique properties or subpopulation, which may also indicate functional abnormalities [68]. To evaluate the system's capability of sorting cells based on the attachment of marker specific beads, we have 1μm diameter fluorescent beads, functionalized with carboxylic groups, randomly bonded to the membrane of Human Embryonic Kidney (HEK-293T) cells and sort cells based on the number of attached beads. To help visualization, the HEK-293T cells are stained with

intracellular carboxyfluorescein dye (CFSE). The example cell images generated by the image-guided cell sorter are shown in Fig 2.5(a). In the sorting experiment, only cells bonded with 3 or more beads are collected. The number of beads attached to each cell is counted in real-time, and the histogram is shown in Fig 2.5(b). The sorting purity was verified by examining 197 fluorescent microscope images of sorted cells, which confirms 96% sorting purity (i.e. 96% of sorted cells contain 3 or more beads bonded to their surface).

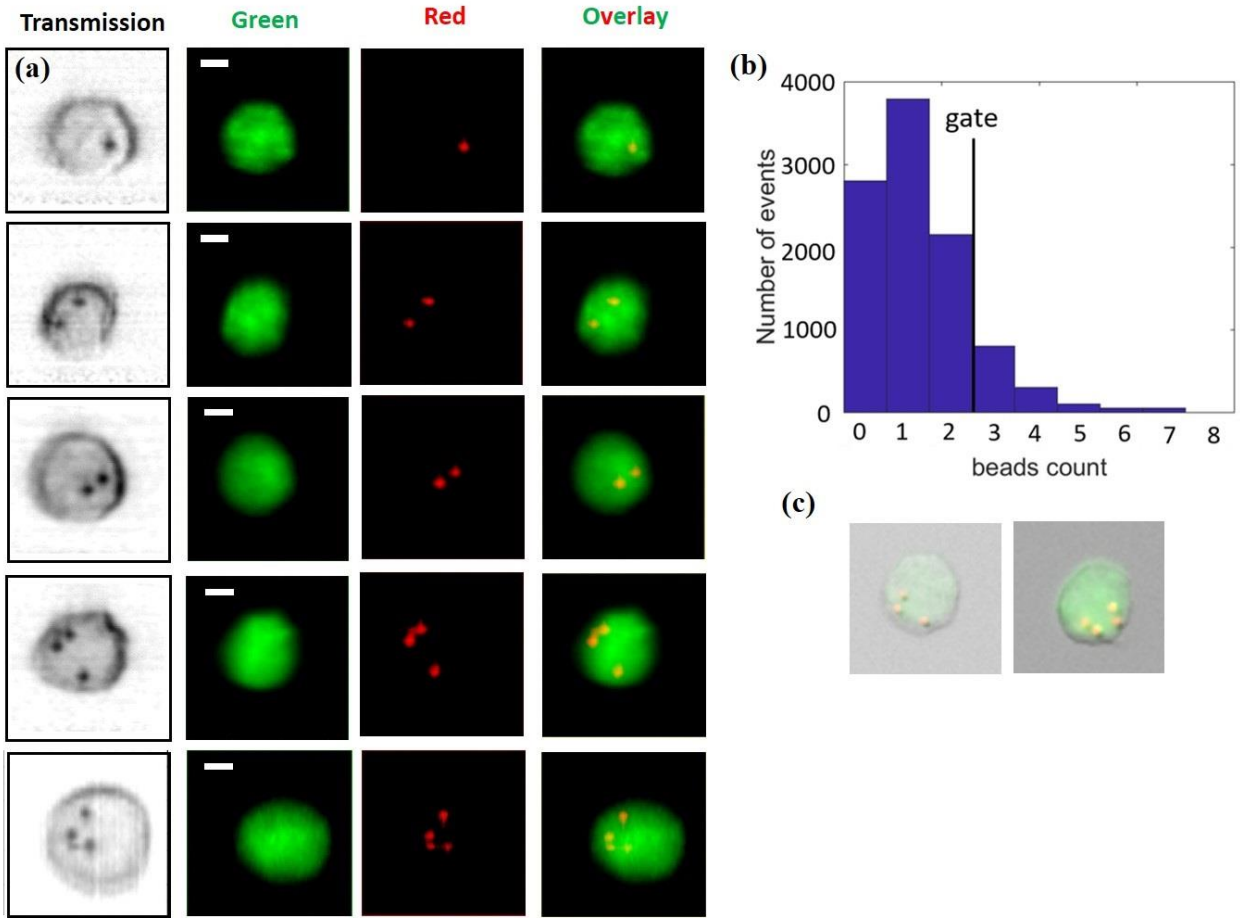

Figure 2.5. Images and histogram of HEK-293T cells bonded with 1μm polystyrene beads. (a) Example images generated by the image-guided cell sorter. First to fourth column: transmission, green fluorescence, red fluorescence, and overlay images. Scale bar: 5μm. (b) Histogram of bead number counted by the image-guided cell sorter. (c) Example microscope images of sorted HEK-293T cells bonded with 3 or more beads.

2.3 Sorting of EGFP-GR Plasmids Translocated HEK-293T Cells

To maintain cell functions and activities, proteins must be transported from cytosol to the correct destination [69]. The localization of specific proteins could be different between normal cells and cancer cells, and abnormal protein translocation can cause cell dysfunction. For example, in normal cells retinoblastoma (RB) tumor suppressor protein is localized in nucleus, but an oncogenic mutation may alter the gene expression pathway and cause delocalization of nuclear RB to cytoplasm [70]. Therefore, detecting and isolating cells according to the spatial distribution of protein has biomedical significance. In the following we demonstrate cell sorting based on the state of protein localization, which cannot be done by conventional FACS because the integrated signal intensity from the labelled protein is not necessarily affected by protein location. We use the image-guided cell sorter to detect and isolate EGFP-GR plasmids translocated HEK-293T cells from un-translocated HEK-293T cells.

Two groups of HEK-293T cells are cultured under the same condition and transfected by the same amount of EGFP-GR, which is localized in cytoplasm. One group of cells is treated with dexamethasone that causes the migration of GR-GFP protein from cytoplasm to nucleus. The 1:1 mixture of these two groups of cells is imaged and the translocated cells are sorted based on the ratio between the GR-GFP protein distribution represented by the fluorescent area and the total cell area from the transmission image. The translocated cells would have a smaller area ratio than un-translocated cells, and the histogram of area ratio is shown in Fig 2.6(b). Same as the previous experiment, the sorting purity is verified by fluorescent microscope images of the sorted cells. We have obtained 100% sorting purity after examining the image of 130 sorted cells.

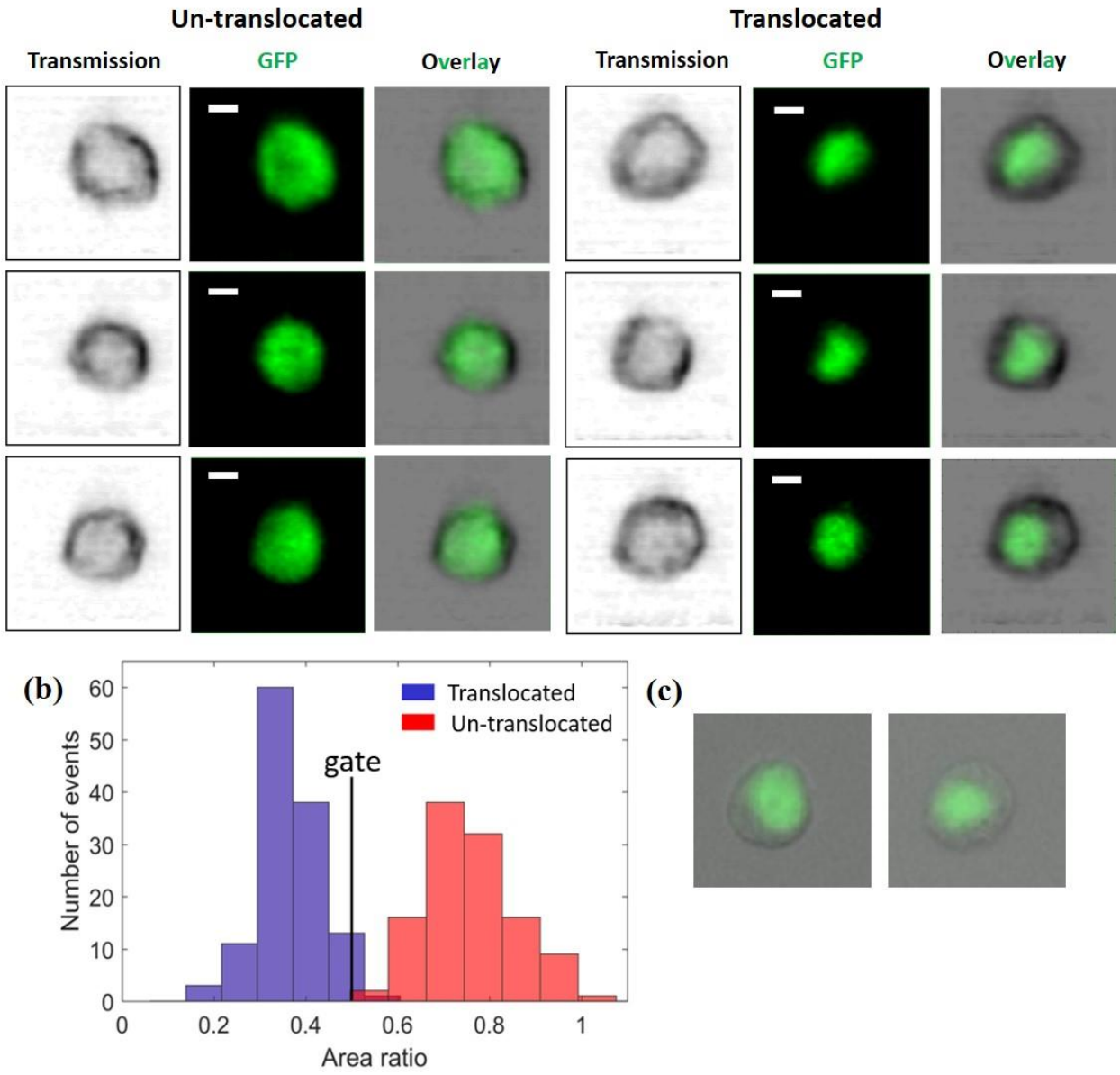

Figure 2.6. Images and histogram of GR-GFP transfected HEK-293T cells. (a) Example transmission, green fluorescence and overlay images generated by image-guided cell sorter. Scale bar: 5μm. (b) Histogram of area ratio, defined by area(fluorescent image) / area(transmission image). (c) Example microscope images of sorted translocated HEK-293T cells.

2.4 Sorting of SKNO-1 Acute Myeloid Leukemia (AML) Cells from Normal White Blood Cells

Leukemia, as one of the most common types of cancer, causes the death of thousands of people every year [71]. Traditional flow cytometers rely on antibody panels to diagnose leukemia cells, which requires costly reagents and a long and tedious process [72]. The image-guided cell sorter offers the possibility of detecting and isolating low concentration of leukemia cells from normal WBCs without antibody or fluorescent labeling, which helps early detection.

In a proof-of-concept experiment, a patient-derived SKNO-1 AML cell line is cultured at 37ºC with 5% CO_2 [73]. These SKNO-1 AML cells are spiked into white blood cells of healthy donors (San Diego Blood Bank, 3636 Gateway Center Ave Suite 100, San Diego). To decide the best sorting criteria for this experiment, we first ran both SKNO-1 cells and WBCs separately to collect cell images, as shown in Fig 2.7(a). A total of 19 features, including area, perimeter, roughness, granularity, contrast, texture, etc., are extracted from these cell images by offline analysis, which concludes that the overall cell area turns out to be the most distinct feature that separates SKNO-1 AML cells from WBCs. The area histogram of SKNO-1 and WBCs in Fig 2.7 I shows that normal WBCs have most of their population in the stationary phase, with an average size of 10μm diameter. For the more frequently dividing SKNO-1 cells, a number of them are expected to be dividing and caught at either mitosis (larger size) or cytokinesis phase (smaller size), so they will have a broader cell size distribution.

To demonstrate the system's ability to sort cells based on label-free image features, ~1-2% of live SKNO-1 cells without fluorescent or antibody labeling are sorted out from live WBCs. Since the apparent area of out-of-focused WBCs may be larger than their actual size, a parameter of "focusing score" is defined to quantify the extent of focus of the cell image, and only the image of cells achieving a sufficiently high focusing score (i.e. >0.5) is analyzed for a sorting decision, as shown in Fig 2.7(f).

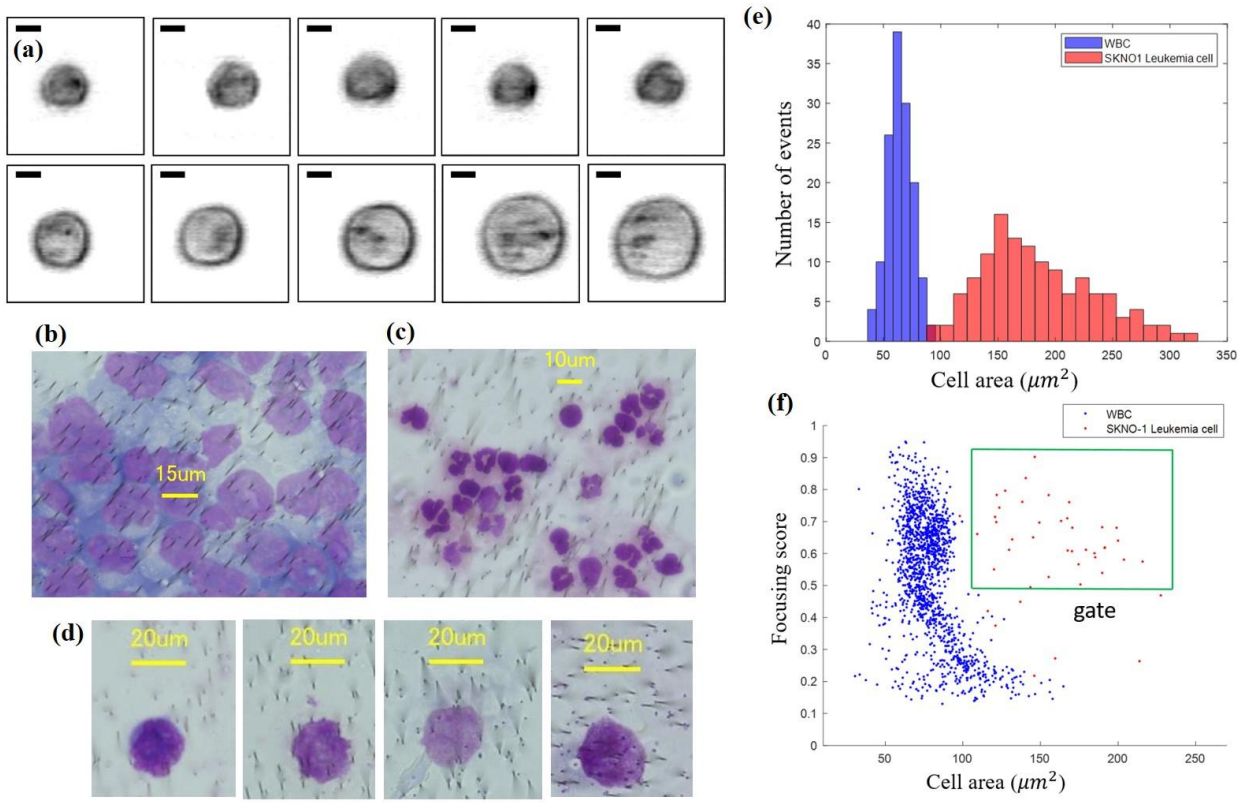

Figure 2.7. (a) Example transmission images generated by image-guided cell sorter. The first row shows the images of normal white blood cells. The second row shows the images of SKNO-1 leukemia cells. Scale bar: 5μm. (b) Wright-Giemsa stain of SKNO-1 leukemia cells on a transparent polyester membrane filter. (c) Wright-Giemsa stain of normal white blood cells on a transparent polyester membrane filter. (d) Example microscope images of SKNO-1 leukemia cells being sorted. (e) Histogram of cell area measured by the image-guided cell sorter. (f) Two-dimensional distribution of cell area and focusing score in real-time sorting experiment. In the sorting experiment, we omit any cells that are poorly focused (i.e. focusing score < 0.5).

To evaluate the sorting performance, we perform Wright-Giemsa staining to WBCs and SKNO-1 leukemia cells. The steps of Wright Giemsa staining can be found in supplementary material. As shown in Figs. 2.7(b) and (c), there is a clear difference between SKNO-1 leukemia cells and WBCs and among different kinds of WBCs after staining. In particular, SKNO-1 leukemia cells are characterized by their irregularly shaped nucleus and larger nucleus to cytoplasm ratio. After the sorting experiment, the collected cells are placed on a polyester transparent membrane filter (1300019, Sterlitech). The stained cells on the membrane filter are

then imaged under bright field by a microscope. After analyzing the image of 251 sorted cells, we have found that 96% of them are SKNO-1 leukemia cells. Considering that the SKNO-1 cells have a relative population of 1-2% initially, the result indicates that the image-guided cell sorter has enriched the SKNO-1 cell population by around 1,200 times in a label-free operation.

3. Conclusion and Discussion

By adopting a design that combines a cameraless imaging technique, microfluidic cartridge with an integrated piezoelectric cell sorter, and real-time image processing and image feature extraction, we have demonstrated an image-guided cell sorting system capable of isolating cells based on their fluorescent and transmission image characteristics. The imaging design uses an AOD controlled dual-color laser scanning system for optical excitation and PMTs for detection of transmitted bright-field and fluorescent signals; and the cell images are obtained by converting the temporal intensity signals into spatial distributions. Cell sorting is directed by the image features of each cell against the defined "image gating", offering much richer information contents for the sorting criteria than conventional intensity-based sorting. Our system can sort cells within the "image gating" into a tube, or sort and dispense each individual cell into one of the wells in a 386-well plate according to the "image gating clusters". For the former operation, the throughput is around 200 cells per second. For the latter, the system can place single cells in a 386-well plate in less than 10 minutes. Various experiments show that our system can consistently achieve sorting purity of over 96% for both labelled and label-free operations. In this paper, we have demonstrated the system's functions for spot counting, protein translocation, and label-free rare cell detection and enrichment. As the trend of combining flow cytometer system and microscopy system continues and biomedicine relies more on image features to understand cell behaviors and find relations between phenotype and genotype, the

ability of cell sorting based on image features marks an important milestone as an enabling tool for the fields of biology and medicine.

The throughput of our system is currently limited by the variations of cell position in the microfluidic channel. With 1D hydrodynamic flow focusing, cells in the microfluidic channel are confined in one direction only and can take different positions in the other direction, the direction along the optical axis. This causes 30 to 40% of cells to be out of focus and produce blurred images. Our current algorithm instructs the system to disregard those cells without sorting to assure high purity, but the process reduces the sorting yield and overall system throughput. At a rate of 400 cells/s entering the system with an average cell speed of 20 cm/s, the current system produces a throughput of 200 cells/s at 5.6% rate of doublets after subtracting 30-40% of the cells that are out of focus and 10-20% cell loss due to tubing connections and interfaces between the microfluidic chip and the cartridge. To overcome these problems, we can produce microfluidic devices with 2D hydrodynamic focusing, improve interface connections between fluidic devices, and extend the focal depth of the scanning laser beam.

Acknowledgements

Chapter 2, in full, is a reprint of the material as it appears in Applied Physics Letter (APL) Photonics. Chen, Xinyu; Gu, Yi; Chen, Jiajie; Lee Chang-Hung; Gagne, Ivan; Tang, Rui; Waller, Lauren; Zhang, Zunming; Zhang Alex C; Han, Yuanyuan; Wang, Weian; Lian Ian Y; Cho, Sung-Hwan; Lo, Yu-Hwa, AIP Publishing, 2020. The dissertation author was the primary researcher and author of this paper.

Chapter 3 LABEL-FREE IMAGE-ENCODED MICROFLUIDIC CELL SORTER WITH A SCANNING BESSEL BEAM

1. Background

In the previous chapter we demonstrated an image-guided cell sorter using a fast-scanning laser as the excitation source. In a simple microfluidic device suitable for low-cost, disposable applications that minimizes cross contamination, one-dimensional flow focusing confines the procession of cells into the center of the microfluidic channel only in one axis perpendicular to the flow direction. In the other perpendicular axis, however, the cell positions are not confined. As a result, particles in the flow channel tend to have a wide distribution in their positions affected by their size, stiffness, shape, and morphology. To extract image related features of high fidelity, keeping the cells at the focal spot of the interrogating beam is essential. Cells positioned outside the focal depth of the interrogating beam will give rise to blurred images. Furthermore, given the typical 10-15 μm cell size, even for the cells located in the focal plane, a significant portion of the cell features can be out of focus. As a result, today's image-guided flow cytometer cell sorters using a tightly focused Gaussian beam from a high numerical aperture (NA) objective face two major challenges: (a) to keep cells of different properties in the flow channel all in focus and (b) to keep all parts of the cells across their thickness along the optical axis in focus. Inability to meet the former requirement gives rise to a large number of out-of-focus cells, resulting in low throughput and biased analysis since some cell subpopulations tend to be in focus more than others. Failure to meet the latter requirement increases the risk of misleading the gating criteria for sorting since the apparent crisp cell image represents only the feature of one cross section of the cell, leaving features outside the focal plane blurry or not

detectable. In this chapter, we demonstrate a scanning Bessel beam system with extended focal depth to overcome the above limits and develop innovative approaches to perform image-guided cell sorting in a disposable microfluidic cartridge. The sorting criteria were directly determined from the image-encoded temporal waveform without image restoration. The system is simple to set up and can operate in a label-free manner.

Although not used in a flow cytometer system before, Bessel beam-based illumination microscopy methods have previously been leveraged to increase the depth of focus in biological specimens with near-isotropic spatial resolution, achieving significant merit in light-sheet microscopy, illumination microscopy, and electron microscopy [74-76]. A Bessel beam is a diffraction-free mode solution of the Helmholtz equation and possesses a number of unique properties which make it useful for imaging applications, including non-diffractive behavior and the ability to self- heal when partially obstructed [77]. A mathematically ideal Bessel beam cannot exist as it is unbounded and carries an infinite amount of energy. An experimentally achievable approximation is to modulate the Bessel beam by a broad width Gaussian function, which is called a Bessel-Gaussian beam. The most used method of generating the Bessel-Gaussian beam is by illuminating a conically shaped element called an axicon with a Gaussian beam [78].

Here we demonstrate an imaging flow cytometer and cell sorter with an ultra-long depth of focus, accomplished by a scanning Bessel-Gaussian laser beam. The two-dimensional cell images can be reconstructed from one dimensional waveform information collected from a PMT. From this waveform, a number of cellular morphological features are quantified, and these values can be used to create appropriate gates for cell sorting. Sorting is accomplished via an integrated PZT as previously described. The PZT-integrated microfluidic device is made of

cyclo-olefin copolymer (COC) material integrated with a cartridge that contains microfluidic channels and interfaces with the fluidic pumps. Both the microfluidic chip and the cartridge are injection molded and can be disposed to eliminate concerns of cross contamination.

Experiments were conducted to evaluate the sorting performance of the system for multiple sizes of polystyrene beads, label-free identification and sorting of acute myeloid leukemia (AML) cells from white blood cells, and the label-free sorting of *Scenedesmus sp*., a green algae, from field-collected microorganisms. Our results indicate a sorting accuracy of 97%, 97%, and 98%, respectively. We also demonstrate an increased percentage of in-focus cell images from 30-40% for a Gaussian beam system to >85% by using a Bessel Gaussian beam, effectively increasing the throughput by about three folds to around 300 cells/second, limited by the response of the on-chip piezoelectric actuator and the presence of cell doublets.

2. Methods

2.1 Design of the Imaging System

The optical system design is shown in Fig. 3.1(a). The Gaussian beam output from a 488nm diode laser illuminates on an axicon (AX1025-A, Thorlabs) with an angle of 0.5º. A Bessel-Gaussian beam is formed by the superposition of two sets of plane waves propagating with a cone angle. The Bessel-Gaussian beam is then modulated by an acousto-optic deflector (OAD948, Isomet). The acoustic transducer deflects the beam to different angles along the y-(scanning) direction at a frequency of 200KHz. Lens1 performs a Fourier transform of the zero order Bessel-Gaussian beam to create an annulus-shaped beam at its focal plane. This annulus-shaped beam is then magnified by lens2 before reaching the exit pupil of a 10X illumination objective lens (378-803-3, Mitutoyo). The illumination objective lens transforms the annulus-shaped beam back to a Bessel-Gaussian beam onto the cells in the microfluidic channel. The

position of the AOD is conjugated with the back focal plane of the objective lens. This schematic creates a fan scan of the laser beam at the front focal plane. The microfluidic chip, which is made of cyclic olefin copolymer (COC) as shown in Fig. 3.1(b), is put at the front focal plane.

Our design uses a single PMT detector and an AOD-scanned CW laser to encode the 2D cell transmission profile into a temporal signal, which can be used as the gating criteria for cell sorting and classification. A spatial mask (mask2 in Fig. 3.1(a)) with one 500μm x 15μm slit is put at the image plane of the 488nm laser channel, which creates a 50μm x 1.5μm transparent area at the focal plane. The slit is aligned to the center of the Bessel-Gaussian beam. As a result, the sidelobes of the Bessel-Gaussian beam along the flow direction are blocked while the sidelobes along the scanning direction can pass the slit.

Since cell speed in the microfluidic channel is position dependent and the speed information is required to correctly relate the temporal waveform to the cell image, we use a 455 nm LED, a PMT, and a spatial mask (mask1 in Fig. 3.1(a)) to detect the speed of each individual cell. The spatial mask contains two 1mm x 10μm slits separated in the cell flow (z-) direction, placed at the image plane of 455nm LED channel. The speed of each cell is obtained by dividing the slit distance with the magnification factor (10x in our case) and the time difference between the minimum in the LED transmission signal. In our experiment, cell speeds are typically between 10 cm/s and 25 cm/s with an average speed of around 20 cm/s.

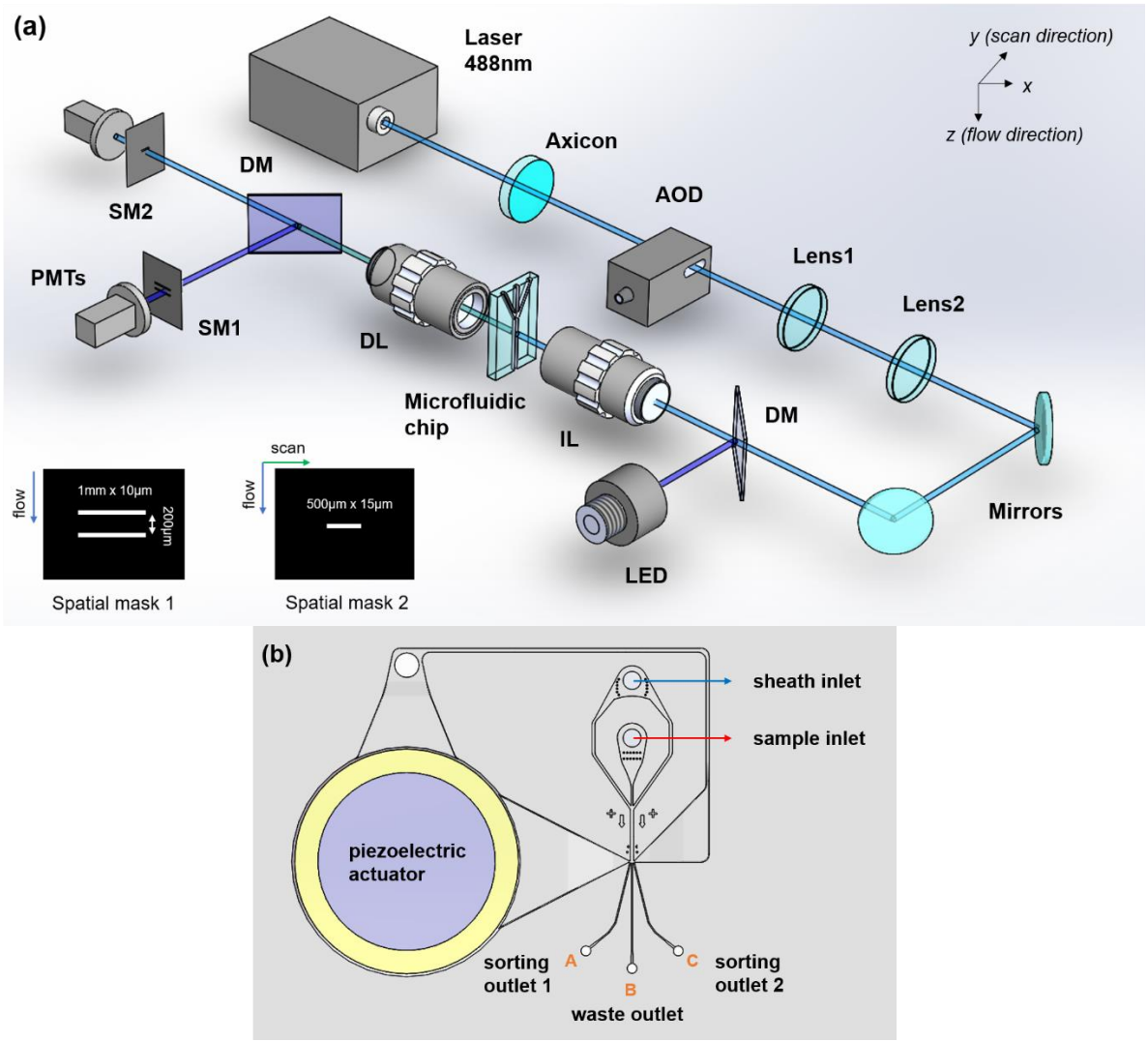

Figure 3.1. (a) Optical imaging system design. AOD, acousto-optic deflector; DM, dichroic mirror; IL, 10×/0.28 illumination objective lens; DL, 10×/0.28 detection objective lens; PMTs, photomultiplier tubes; and SM: spatial filter. The spatial masks for cell speed detection and transmission imaging are shown on the bottom left. (b) Microfluidic chip design. The chip is made of cyclic olefin copolymer (COC) by injection molding.

The microfluidic sorting chip was made of COC (Cyclic Olefin Copolymer) by injection molding. COC was chosen due to its high transparency in the visible wavelength, low autofluorescence, and low fabrication cost. The piezoelectric actuator was attached to the top of the COC microchip via a thin layer of double-sided pressure sensitive adhesive (PSA). The sample stream is focused by the sheath flow hydrodynamically. When a target cell is detected,

the piezo-actuator is triggered to push or pull the target cell to sorting outlet 1 or 2 and eventually into either the collection tubes or specific wells in a 384-well plate. Cells that are not of interest travel through the center channel to the waste outlet.

2.2 Simulation of the Bessel Gaussian Beam Transmission Signal

To gain insight into the transmission of a Bessel Gaussian beam through an object, we use COMSOL Multiphysics simulation software to show how a 7μm bead (n=1.6) changes the optical intensity distribution of a Bessel-Gaussian beam (Fig. 3.2). Since our system measures the far field of the transmitted light, we simulate the electric field distribution 400μm away from the bead to satisfy the Fraunhofer far-field condition. When there is no object in the interrogation zone, the laser light transmits through the slit and generates a constant DC background. When the laser beam intersects the bead, the light will be partially reflected and partially diffracted. If the diffraction angle θ is greater than the collection angle of the detection objective lens, the light intensity on the PMT decreases, resulting in a dark region in the transmission image of the 7μm bead due to the combined effects of reflection and diffraction assuming the effect of light absorption is negligible. According to the simulation, when the Bessel-Gaussian beam hits the center of the 7μm bead, the calculated diffraction angle θ is around 2 degrees, much smaller than the collection angle of the detection objective (10X, NA=0.28). Thus, the small angle diffraction beam can pass the slit and reach the PMT, producing a “bright spot” at the center of the image of the bead. This explains why we observe a bright spot at the center of the restored bead image from the transmitted signal (Fig. 3.2(b)). As a general rule, areas of large optical density and large angle scattering give rise to dark regions; and areas of low optical density and small angle scattering give rise to bright regions in the restored transmission images.

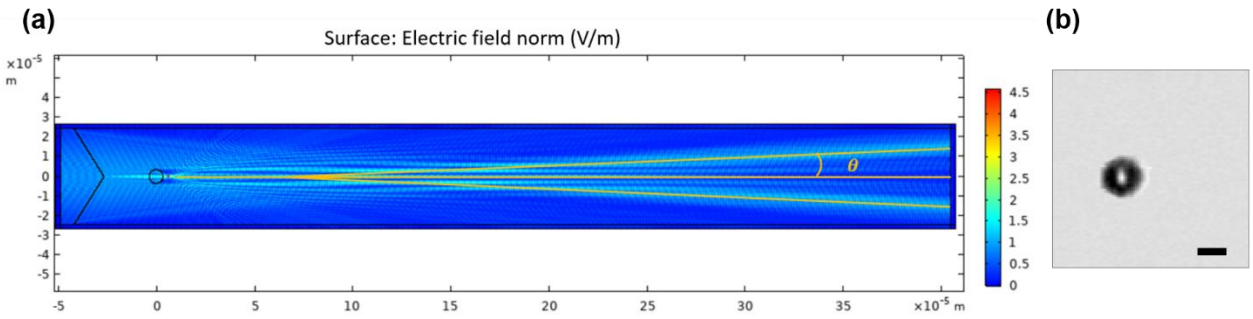

Figure 3.2. (a) COMSOL simulation of the electric field when a Bessel-Gaussian beam illuminates on the center of a 7μm bead. (b) Example transmission image of a 7μm bead generated by the image-guided cell sorter using a scanning Bessel-Gaussian beam. The image was reconstructed using the mathematical algorithm discussed in Section D. Scale bar: 5μm.

2.3 Depth of Focus Comparison

As discussed previously, the main motive of using a Bessel Gaussian beam to replace a Gaussian beam is to extend the focal depth such that objects in different positions in a microfluidic channel and different cross sections of the cell can all be focused to generate high fidelity 2D cell image information. Fig 3.3 shows the intensity profile and focal depth of the Bessel Gaussian beam measured by a camera. Fig 3.3(a) and (b) show the intensity profile of the Bessel Gaussian beam at the image plane. The full width half maximum (FWHM) of the center lobe is between 1μm and 1.5μm. As expected, a significant amount of energy is in the side lobes, which excite areas outside the central spot and complicate the waveform analysis when we use a single PMT for detection to keep the system simple and at low cost. A mathematical algorithm to be discussed in the next section is required to deconvolve the signal when we reconstruct the transmission image. To measure the focal depth, beam profiles at different depths are recorded by moving the detection objective lens along the beam propagation (x-) direction. Both the maximum intensity and FWHM of the center lobe have relatively small changes within a distance of 160μm, as shown in Fig. 3.3(c). In contrast, a Gaussian beam produced by the same objective lens has a much shorter focal depth of about 7.37μm.

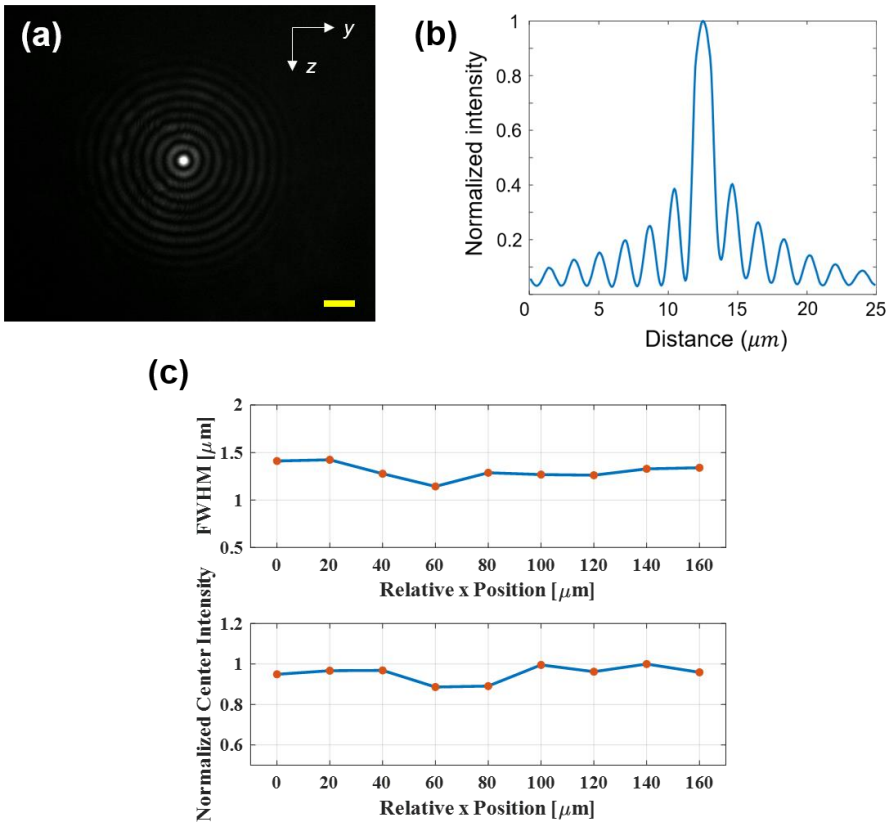

Figure 3.3. Bessel-Gaussian beam profile. (a) Camera measured beam profile at the image plane. (b) Normalized intensity from the center of the Bessel-Gaussian beam. (c) Full-width-half-maximum and normalized light intensity of the main lobe of Bessel-Gaussian beam.

To assess how the extended focal depth of a Bessel-Gaussian beam can improve the detection yield compared to a Gaussian beam, we ran a mixture of cells and beads, including 15µm beads, 7µm beads, HEK 293T cells, MCF7 cells and Hela cells, in both Gaussian beam and Bessel-Gaussian beam image-guided cell sorters. The results are summarized in Table 3.1. In the Gaussian beam system, the short focal depth cannot keep the majority of objects in focus due to the wide distribution of the objects along the microfluidic channel. Except for 15µm beads that tend to take a stable position in the channel, only 30-40% 7µm beads, and only 40-60% cells are in focus. In sharp contrast, > 90% of 7µm beads, 98% of 15µm beads, and 85% of the cells of all kinds are in focus in the Bessel-Gaussian beam system.

Fig 3.4 shows example in-focus and out-of-focus 15μm bead and 7μm bead images generated by the Gaussian beam system. In sharp contrast, the vast majority of both 15μm and 7μm diameter beads are well focused for the Bessel-Gaussian beam system.

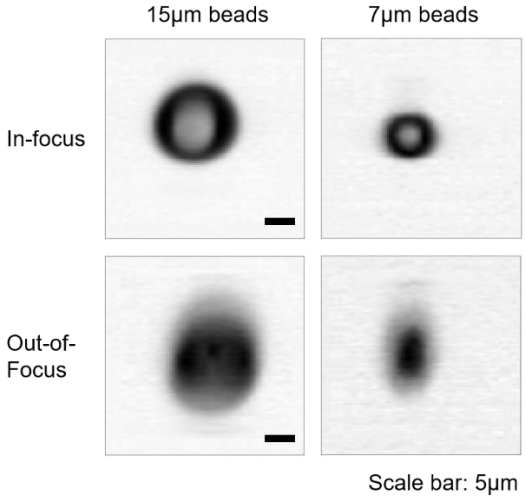

Figure 3.4. Examples of in-focus (first row) and out-of-focus (second row) images for 15μm and 7μm beads, generated by a scanning Gaussian beam image-guided cell sorter. In comparison, nearly all images from the scanning Bessel Gaussian beam system are well in focus (see Fig. 3.5). Scale bar: 5μm.

Table 3.1. Comparison of the ratio of in-focus objects between the scanning Gaussian beam system and the scanning Bessel-Gaussian beam system.

	Gaussian System	Bessel-Gaussian System
7μm beads	30%-40%	90%-95%
15μm beads	~98%	~98%
Cell Mixture	40%-60%	85%-90%

2.4 Image reconstruction algorithm

In this section we describe the mathematical algorithm to reconstruct images from the label-free, transmission signal by a Bessel Gaussian beam. It is noted that because of the

correlation between the PMT temporal signal and the image features, we do not need to use the restored cell images as gates to sort cells. Instead, we sort cells directly from the features in the waveform, thus saving time and resources for real time signal processing. Therefore, image reconstruction can be performed off-line for validation of the results and improved human-machine interface when users would like to observe image differences between sorted and unsorted cells and visualize image related features such as size, shape, granularity, contrast, etc.

The electric field of Bessel-Gaussian beam:

$$E_{BG}(r,x) \sim E_0 J_0(k_r r) \frac{w_0}{w(x)} e^{-\frac{r^2}{w_0^2}} \cdot e^{-ik_x x} e^{-i\emptyset} \qquad (3.1)$$

where $r = \sqrt{y^2 + z^2}$ is the distance from the center of the Bessel Gaussian beam. E_0 is a field amplitude constant. k_r is the wavevector in the transverse plane and ${k_r}^2 + {k_x}^2 = k^2$. w_0 is the waist width of Gaussian amplitude. $\emptyset = tan^{-1}\frac{x}{x_0}$. x_0 is Rayleigh length of the Gaussian beam.

We use $n(x,y,z)$ to denote the cell or bead index profile $n(x,y,z) = n_o + \Delta n(x,y,z)$. We assume n_o is the index of water and $\Delta n > 0$ since the index of cells and beads is greater than the index of water. Assume cell or bead thickness is within x_c. For the 2D imaging system, we cannot resolve index change along the beam propagation direction, so we make the following approximation:

$$\int_0^{x_c} \Delta n(x,y,z)dx = \Delta\bar{n}(y,z)x_c \qquad (3.2)$$

Adding a slit in parallel with the laser scanning (y-) direction on the image plane and assuming the slit is narrow enough to be approximated by a 1-D delta function in its transmission characteristic, the transmitted field focused by a lens and after the slit can be approximated by (3.3).

$$E_t(y',z') = E_0' e^{-ik_o x} e^{-i\emptyset} \frac{w_0}{w(x)} \int_y^{\square} \int_z^{\square} \delta(z - z') \left(\frac{2\sqrt{n_o(n_o+\Delta\bar{n}(y,z)}}{2n_o+\Delta\bar{n}(y,z)}\right) J_0\left[k_r\sqrt{(y'-y)^2+(z'-z)^2}\right] e^{-\frac{(y'-y)^2+(z'-z)^2}{w_0^2}} e^{-ik_o\Delta\bar{n}(y,z)x_c} dydz \quad (3.3)$$

The term $\left(\frac{2\sqrt{n_o(n_o+\Delta\bar{n}(y,z)}}{2n_o+\Delta\bar{n}(y,z)}\right)$ in Eq. (3.3) is the approximate transmission coefficient assuming there is no absorption. Here (y,z) refers to the transverse coordinate in the object plane, and (y',z') refers to the transverse coordinate in the image (detection) plane. For simplicity, we have transformed the actual position (Y',Z') in the image plane into (y',z') by defining $y' = \frac{Y'}{M}$ and $z' = \frac{Z'}{M}$ with M being the magnification of the detection optics.

Also note that (y',z') is related to time by the following relations:

$$y' = \frac{FOV_y}{T}\, t \qquad (3.4\text{-a})$$

$$z' = v_{cell} t \qquad (3.4\text{-b})$$

From the relations in Eq.(3.4), we can relate a signal in time domain to the space domain, thus reconstructing the image from a temporal waveform.

To analyze the detected cell transmission signal behind the slit when the center of the scanning Bessel Gaussian beam is at a given position in the flow (z'-) direction, we can represent the transmitted field in (3.5) under a given position z'.

$$E_t(y')|_{z'} \propto \int_y^{\square} \left(\frac{2\sqrt{n_o(n_o+\Delta\bar{n}(y)|_{z'}}}{2n_o+\Delta\bar{n}(y)|_{z'}}\right) J_0\left[k_r\sqrt{(y'-y)^2}\right] e^{-\frac{(y'-y)^2}{w_0^2}} e^{-ik_o\Delta\bar{n}(y)|_{z'}x_c} dy \qquad (3.5)$$

Equation (3.5) shows that $E_t(y')|_{z'}$ is the convolution of the index function $\left(\frac{2\sqrt{n_o(n_o+\Delta\bar{n}(y)|_{z'}}}{2n_o+\Delta\bar{n}(y)|_{z'}}\right) e^{-ik_o\Delta\bar{n}(y)|_{z'}x_c}$ and the Bessel Gaussian function $J_0[k_r y] e^{-\frac{y^2}{w_0^2}}$ along the scanning (y-) direction. To save computational power for image reconstruction, we approximate the Bessel function $J_0[k_r y]$ by a series of delta functions at its maxima and minima (Fig. 3.5):

$$J_o(u) \sim \sum_m c_{max,m}\delta(u - u_{max,m}) + \sum_n c_{min,n}\delta(u - u_{min,n}) \qquad (3.6)$$

$u_{max,m}$: positions of *mth* maximum of $J_o(u)$. $J_o(u_{max,m}) > 0;\ \ m = 0, \pm1, \pm2, \pm3, \cdots$

$u_{min,n}$: positions of *nth* minimum of $J_o(u)$. $J_o(u_{min,n}) < 0;\ \ n = \pm1, \pm2, \pm3, \cdots$

The coefficients for each delta function are defined as

$$c_{max,m} = J_0(u_{max,m}) \qquad m = 0, \pm1, \pm2, \pm3, \cdots$$

$$c_{min,n} = J_0(u_{min,n}) \qquad n = \pm1, \pm2, \pm3, \cdots \qquad (3.7)$$

Substituting (3.6) and (3.7) into (3.5) and dropping the parameter z' for simplicity, we obtain the following approximate expression of the transmitted E-field behind the slit,

$$E_t(y')|_{z'} \sim \left[\sum_m C_{max,m} exp\left[-\frac{u_{max,m}^2}{(k_r w_o)^2}\right]\left(\frac{2\sqrt{n_o(n_o+\Delta\bar{n}\left(y'-\frac{u_{max,m}}{k_r}\right)|_{z'}}}{2n_o+\Delta\bar{n}\left(y'-\frac{u_{max,m}}{k_r}\right)|_{z'}}\right) e^{-ik_o\Delta\bar{n}\left(y'-\frac{u_{max,m}}{k_r}\right)|_{z'}x_c}\right] -$$
$$\left[\sum_n C_{min,n} exp\left[-\frac{u_{min,n}^2}{(k_r w_o)^2}\right]\left(\frac{2\sqrt{n_o(n_o+\Delta\bar{n}\left(y'-\frac{u_{min,n}}{k_r}\right)|_{z'}}}{2n_o+\Delta\bar{n}\left(y'-\frac{u_{min,n}}{k_r}\right)|_{z'}}\right) e^{-ik_o\Delta\bar{n}\left(y'-\frac{u_{min,n}}{k_r}\right)|_{z'}x_c}\right] \qquad (3.8)$$

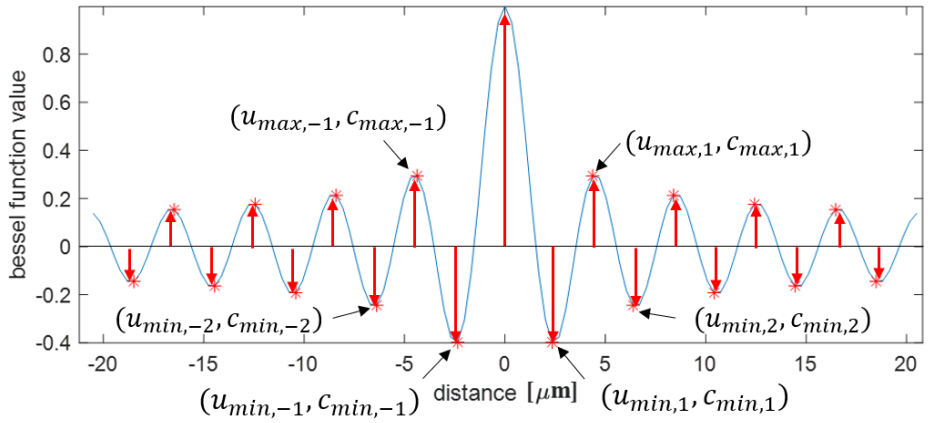

Figure 3.5. Approximate a Bessel function by a series of delta functions at the maxima and minima. $u_{max,m}$ and $u_{min,n}$ are positions of mth maximum and nth minimum of $J_o(u)$. $c_{max,m} = J_0(u_{max,m})$, $c_{min,n} = J_0(u_{min,n})$.

Representing $E_t(y') \sim A - B$ in brief form, we can write the transmitted power through the slit as:

$$J_t(y')|_{z'} \propto E_t^*(y')|_{z'} E_t(y')|_{z'} \propto AA^* + BB^* - AB^* - BA^* \qquad (3.9)$$

Next, we analyze each term in (3.9):

$$AA^*(y')\sim\left[\cdot\left(\frac{2\sqrt{n_o(n_o+\Delta\bar{n}\left(y'-\frac{u_{max,m}}{k_r}\right)|_{z'}}}{2n_o+\Delta\bar{n}\left(y'-\frac{u_{max,m}}{k_r}\right)|_{z'}}\right)\left(\frac{2\sqrt{n_o(n_o+\Delta\bar{n}\left(y'-\frac{u_{max,m'}}{k_r}\right)|_{z'}}}{2n_o+\Delta\bar{n}\left(y'-\frac{u_{max,m'}}{k_r}\right)|_{z'}}\right)\right]\cdot \sum_{m,m'} C_{max,m}\, C_{max,m'} exp\left[-\frac{u_{max,m}^2+u_{max,m'}^2}{(k_r w_o)^2}\right]$$
$$e^{-ik_o[\Delta\bar{n}\left(y'-\frac{u_{max,m}}{k_r}\right)-\Delta\bar{n}\left(y'-\frac{u_{max,m'}}{k_r}\right)]x_c} \qquad (3.10)$$

It can be shown that the imaginary part of AA^* is zero. Thus

$$AA^*(y')\sim\left[\cdot\left(\frac{2\sqrt{n_o(n_o+\Delta\bar{n}\left(y'-\frac{u_{max,m}}{k_r}\right)|_{z'}}}{2n_o+\Delta\bar{n}\left(y'-\frac{u_{max,m}}{k_r}\right)|_{z'}}\right)\left(\frac{2\sqrt{n_o(n_o+\Delta\bar{n}\left(y'-\frac{u_{max,m'}}{k_r}\right)|_{z'}}}{2n_o+\Delta\bar{n}\left(y'-\frac{u_{max,m'}}{k_r}\right)|_{z'}}\right)\right]\cdot \sum_{m,m'} C_{max,m}\, C_{max,m'} exp\left[-\frac{u_{max,m}^2+u_{max,m'}^2}{(k_r w_o)^2}\right]$$
$$\cdot cos\left[k_o[\Delta\bar{n}\left(y'-\frac{u_{max,m}}{k_r}\right)-\Delta\bar{n}\left(y'-\frac{u_{max,m'}}{k_r}\right)]x_c\right] \qquad (3.10\text{-a})$$

For $m \neq m'$, the summation of the phase mismatched terms in Eq.(3.10-a) leads to cancellation and produce small effects. Keeping the $m = m'$ terms only and having $u_{max,m=0} = 0$ (i.e. the first max for the zero-order Bessel function is at the origin).

$$AA^*(y') \cong \frac{4n_o(n_o+\Delta\bar{n}(y')|_{z'}}{(2n_o+\Delta\bar{n}(y')|_{z'})^2} + \left[\sum_{m\neq 0} C_{max,m}{}^2\, exp\left[-\frac{2u_{max,m}^2}{(k_r w_o)^2}\right]\frac{4n_o(n_o+\Delta\bar{n}\left(y'-\frac{u_{max,m}}{k_r}\right)|_{z'}}{\left(2n_o+\Delta\bar{n}\left(y'-\frac{u_{max,m}}{k_r}\right)|_{z'}\right)^2}\right] \qquad (3.10\text{-b})$$

Similarly, we have

$$BB^*(y')\sim\left[\cdot\left(\frac{2\sqrt{n_o(n_o+\Delta\bar{n}\left(y'-\frac{u_{min,n}}{k_r}\right)|_{z'}}}{2n_o+\Delta\bar{n}\left(y'-\frac{u_{min,n}}{k_r}\right)|_{z'}}\right)\left(\frac{2\sqrt{n_o(n_o+\Delta\bar{n}\left(y'-\frac{u_{min,n'}}{k_r}\right)|_{z'}}}{2n_o+\Delta\bar{n}\left(y'-\frac{u_{min,n'}}{k_r}\right)|_{z'}}\right)\right]\cdot \sum_{n,n'} C_{min,n}\, C_{min,n'} exp\left[-\frac{u_{min,n}^2+u_{min,n'}^2}{(k_r w_o)^2}\right]$$
$$e^{-ik_o[\Delta\bar{n}\left(y'-\frac{u_{min,n}}{k_r}\right)-\Delta\bar{n}\left(y'-\frac{u_{min,n'}}{k_r}\right)]x_c} \qquad (3.11)$$

$$BB^*(y')\sim\left[\cdot\left(\frac{2\sqrt{n_o(n_o+\Delta\bar{n}\left(y'-\frac{u_{min,n}}{k_r}\right)|_{z'}}}{2n_o+\Delta\bar{n}\left(y'-\frac{u_{min,n}}{k_r}\right)|_{z'}}\right)\left(\frac{2\sqrt{n_o(n_o+\Delta\bar{n}\left(y'-\frac{u_{min,n'}}{k_r}\right)|_{z'}}}{2n_o+\Delta\bar{n}\left(y'-\frac{u_{min,n'}}{k_r}\right)|_{z'}}\right)\right] \quad cos\left[k_o[\Delta\bar{n}\left(y'-\frac{u_{min,n}}{k_r}\right)-\Delta\bar{n}\left(y'-\frac{u_{min,n'}}{k_r}\right)]x_c\right] \qquad (3.11\text{-a})$$

For the same argument as before, we take only the terms where $n = n'$, then Eq.(3.11-a) can be represented approximately as

$$BB^*(y') \cong \left[\sum_n {C_{min,n}}^2 \, exp\left[-\frac{2u_{min,n}^2}{(k_r w_o)^2}\right] \frac{4n_o(n_o+\Delta\bar{n}\left(y'-\frac{u_{min,n}}{k_r}\right)|_{z'}}{\left(2n_o+\Delta\bar{n}\left(y'-\frac{u_{min,n}}{k_r}\right)|_{z'}\right)^2}\right] \qquad (3.11\text{-b})$$

Similarly,

$$AB^*(y') \sim \left[\cdot \left(\frac{2\sqrt{n_o(n_o+\Delta\bar{n}\left(y'-\frac{u_{max,m}}{k_r}\right)|_{z'}}}{2n_o+\Delta\bar{n}\left(y'-\frac{u_{max,m}}{k_r}\right)|_{z'}}\right)\left(\frac{2\sqrt{n_o(n_o+\Delta\bar{n}\left(y'-\frac{u_{min,n'}}{k_r}\right)|_{z'}}}{2n_o+\Delta\bar{n}\left(y'-\frac{u_{min,n'}}{k_r}\right)|_{z'}}\right)\right] \cdot$$

$$\sum_{m,n'} C_{max,m}\, C_{min,n'} exp\left[-\frac{u_{max,m}^2+u_{min,n'}^2}{(k_r w_o)^2}\right]$$

$$e^{-ik_o[\Delta\bar{n}\left(y'-\frac{u_{max,m}}{k_r}\right)-\Delta\bar{n}\left(y'-\frac{u_{min,n\prime}}{k_r}\right)]x_c} \qquad (3.12)$$

$$AB^*(y') \sim \left[\cdot \left(\frac{2\sqrt{n_o(n_o+\Delta\bar{n}\left(y'-\frac{u_{max,m}}{k_r}\right)|_{z\prime}}}{2n_o+\Delta\bar{n}\left(y'-\frac{u_{max,m}}{k_r}\right)|_{z\prime}}\right)\left(\frac{2\sqrt{n_o(n_o+\Delta\bar{n}\left(y'-\frac{u_{min,n\prime}}{k_r}\right)|_{z\prime}}}{2n_o+\Delta\bar{n}\left(y'-\frac{u_{min,n}{}'}{k_r}\right)|_{z\prime}}\right)\right]$$

$$\sum_{m,n'} C_{max,m}\, C_{min,n'} exp\left[-\frac{u_{max,m}^2+u_{min,n\prime}^2}{(k_r w_o)^2}\right]$$

$$\cdot cos\left[k_o[\Delta\bar{n}\left(y'-\frac{u_{max,m}}{k_r}\right)-\Delta\bar{n}\left(y'-\frac{u_{min,n\prime}}{k_r}\right)]x_c\right] \quad (3.12\text{-a})$$

For the same argument as above, we have $AB^*(y') \sim 0$, since the cos terms contain random phases.

$$BA^*(y') \sim \left[\cdot \left(\frac{2\sqrt{n_o(n_o+\Delta\bar{n}\left(y'-\frac{u_{min,n}}{k_r}\right)|_{z'}}}{2n_o+\Delta\bar{n}\left(y'-\frac{u_{min,n}}{k_r}\right)|_{z'}}\right)\left(\frac{2\sqrt{n_o(n_o+\Delta\bar{n}\left(y'-\frac{u_{max,m'}}{k_r}\right)|_{z'}}}{2n_o+\Delta\bar{n}\left(y'-\frac{u_{max,m}{}'}{k_r}\right)|_{z'}}\right)\right]$$

$$\sum_{n,m'} C_{min,n}\, C_{max,m'} exp\left[-\frac{u_{min,n}^2+u_{max,m'}^2}{(k_r w_o)^2}\right]$$

$$e^{-ik_o[\Delta\bar{n}\left(y'-\frac{u_{min,n}}{k_r}\right)-\Delta\bar{n}\left(y'-\frac{u_{max,m\prime}}{k_r}\right)]x_c} \qquad (3.13)$$

For the same reason above, $BA^*(y') \sim 0$.

As a result, we have

$$J_t(y',x) \sim \frac{4n_o(n_o+\Delta\bar{n}(y')|_{z'}}{(2n_o+\Delta\bar{n}(y')|_{z'})^2} + \left[\sum_{m\neq 0} {C_{max,m}}^2 \, exp\left[-\frac{2u_{max,m}^2}{(k_r w_o)^2}\right] \frac{4n_o(n_o+\Delta\bar{n}\left(y'-\frac{u_{max,m}}{k_r}\right)|_{z'}}{\left(2n_o+\Delta\bar{n}\left(y'-\frac{u_{max,m}}{k_r}\right)|_{z'}\right)^2}\right] +$$

$$\left[\sum_n {C_{min,n}}^2 \, exp\left[-\frac{2u_{min,n}^2}{(k_r w_o)^2}\right] \frac{4n_o(n_o+\Delta\bar{n}\left(y'-\frac{u_{min,n}}{k_r}\right)|_{z'}}{\left(2n_o+\Delta\bar{n}\left(y'-\frac{u_{min,n}}{k_r}\right)|_{z'}\right)^2}\right] \quad (3.14)$$

Define $f(y,z) = \frac{4n_o(n_o+\Delta\bar{n}(y)}{(2n_o+\Delta\bar{n}(y))^2}|_z$. By solving $f(y,z)$, we can obtain the index profile of the object $\Delta\bar{n}(y,z)$.

According to (3.14), we have

$$J_t(y',z') = f(y',z') + \left[\sum_{m\neq 0} {C_{max,m}}^2 \, exp\left[-\frac{2u_{max,m}^2}{(k_r w_o)^2}\right] f\left(y' - \frac{u_{max,m}}{k_r}, z'\right)\right] + \left[\sum_n {C_{min,n}}^2 \, exp\left[-\frac{2u_{min,n}^2}{(k_r w_o)^2}\right] f\left(y' - \frac{u_{min,n}}{k_r}, z'\right)\right]$$

$$= f(y',z') + \left[\sum_{m\neq 0} {a_{max,m}}^2 f\left(y' - \frac{u_{max,m}}{k_r}, z'\right)\right] + \left[\sum_n {a_{min,n}}^2 f\left(y' - \frac{u_{min,n}}{k_r}, z'\right)\right] \qquad (3.15)$$

$${a_{max,m}}^2 = {C_{max,m}}^2 e^{-\frac{2{u_{max,m}}^2}{k_r^2 W_o^2}} \qquad m = \pm 1, \pm 2, \pm 3, \cdots \qquad (3.16\text{-a})$$

$${a_{min,m}}^2 = {C_{min,n}}^2 e^{-\frac{2{u_{min,n}}^2}{k_r^2 W_o^2}} \qquad n = \pm 1, \pm 2, \pm 3, \cdots \qquad (3.16\text{-b})$$

Next, we discuss how to determine the limits of m and n in (S15). We assume the scanning range of the laser beam is from $-L_y/2$ to $L_y/2$, and the laser beam spot covers a range from $-W_y/2$ to $+W_y/2$ due to the side lobes of the Bessel Gaussian beam. Assume a scanning rate of 200kHz and a sampling rate of 25 MS/s, we have 125 sampling points for each scan corresponding to the beam center position.

We assume the width of the side lobes of a Bessel Gaussian beam is W_y. The transmitted light intensity becomes nonzero when $-\frac{W_y}{2} < y' - y < \frac{W_y}{2}$. Then

$$-\frac{L_y}{2} - \frac{W_y}{2} < y < \frac{L_y}{2} + \frac{W_y}{2} \qquad (3.17)$$

Equation (3.17) defines the integration range for (3.15). In other words, we need to integrate at least over this range defined in (3.17) to restore the object image from the measured data in each scan.

The dimension of the T-matrix we will discuss next would be a $\left\{125\left[1+\frac{W_y}{L_y}\right]+1\right\} \times \left\{125\left[1+\frac{W_y}{L_y}\right]+1\right\}$ matrix. If we choose $\frac{W_y}{L_y} = 1$, then the T-matrix is a 251x251 matrix.

We write $J_t(y', z')$ into a column matrix with 125 non-zero elements defined by the "width" of the Bessel Gaussian beam. Arbitrarily, we choose these 125 nontrivial points in an index range from -2 to 122, as shown in (3.18). Outside this range, we define the "padding values" $B = J_t(y'_0, z')$ and $B' = J_t(y'_{120}, z')$.

$$\begin{bmatrix} B \\ \cdots \\ B \\ J_t(y'_{-2}, z') \\ J_t(y'_{-1}, z') \\ J_t(y'_0, z') \\ J_t(y'_1, z') \\ J_t(y'_2, z') \\ \vdots \\ J_t(y'_{120}, z') \\ J_t(y'_{121}, z') \\ J_t(y'_{122}, z') \\ B' \\ B' \\ \cdots \\ B' \end{bmatrix}_{251x1} = [T]_{251x251} \begin{bmatrix} f(y'_{-65}, z') \\ \cdots \\ f(y'_{-3}, z') \\ f(y'_{-2}, z') \\ f(y'_{-1}, z') \\ f(y'_0, z') \\ f(y'_1, z') \\ f(y'_2, z') \\ \vdots \\ f(y'_{120}, z') \\ f(y'_{121}, z') \\ f(y'_{122}, z') \\ f(y'_{123}, z') \\ f(y'_{124}, z') \\ \cdots \\ f(y'_{185}, z') \end{bmatrix}_{251x1} \quad (3.18)$$

$J_t(y'_0, z'), \cdots, J_t(y'_{120}, z')$ and $f(y'_0, z'), \cdots, f(y'_{120}, z')$ are within the "chosen" field of view. $J_t(y'_{-2}, z'), J_t(y'_{-1}, z'), J_t(y'_{121}, z'), J_t(y'_{122}, z')$ are measured signal within the laser scanning range. The reason why we have nontrivial $f(y'_{-65}, z'), \cdots, f(y'_{-3}, z')$ and $f(y'_{123}, z'), \cdots, f(y'_{185}, z')$ is because the side lobes of the Bessel Gaussian beam can illuminate objects outside the field of view.

Calculating the inverse of the T-matrix, we can solve $f(y', z')$

$$\begin{bmatrix} f(y'_{-65}, z') \\ \cdots \\ f(y'_{-3}, z') \\ f(y'_{-2}, z') \\ f(y'_{-1}, z') \\ f(y'_{0}, z') \\ f(y'_{1}, z') \\ f(y'_{2}, z') \\ \vdots \\ f(y'_{120}, z') \\ f(y'_{121}, z') \\ f(y'_{122}, z') \\ f(y'_{123}, z') \\ f(y'_{124}, z') \\ \cdots \\ f(y'_{185}, z') \end{bmatrix}_{251x1} = [T]^{-1}_{251x251} \begin{bmatrix} B \\ \cdots \\ B \\ J_t(y'_{-2}, z') \\ J_t(y'_{-1}, z') \\ J_t(y'_{0}, z') \\ J_t(y'_{1}, z') \\ J_t(y'_{2}, z') \\ \vdots \\ J_t(y'_{120}, z') \\ J_t(y'_{121}, z') \\ J_t(y'_{122}, z') \\ B' \\ B' \\ \cdots \\ B' \end{bmatrix}_{251x1} \quad (3.19)$$

The elements of the T-matrix are defined as follow:

$$T_{ij} = 1. \quad if \quad i = j, \quad -65 \le i, j \le 185$$

$$T_{ij} = {C_l}^2 exp\left[-\frac{2u_l^2}{(k_r w_o)^2}\right] \equiv a_l^2 \text{ where } u_l \text{ is the } lth\ min \text{ or } max \text{ for } J_0(u) \text{ if } y'_i - \frac{u_l}{k_r} = y'_j$$

$$T_{ij} = 0. \quad otherwise \quad (3.20)$$

Equations (3.19) and (3.20) describe how we reconstruct the transmission images for cells or beads from the PMT signal.

2.5 Waveform-Based Real-Time Sorting

The mathematical algorithm in the previous section can recover the object image from the PMT signal. However, the computation of 251x251 matrix multiplication is time-consuming and can limit the throughput. On the other hand, because most cell features, including size, spottiness, granularity, etc., are encoded in the PMT output waveform, we can extract many image features that differentiate cell types directly from the temporal waveform without reconstructing the 2D cell images. This saves tremendous computation time and resources, and

the method is suitable for cell sorting by image features. For all sorting experiments reported in this paper, we define gating based on the characteristics of the temporal waveform, which are closely correlated to specific image features. We then use the mathematical algorithm discussed in the previous section to reconstruct the cell transmission images off-line for verification purposes. To quantify sorting accuracy, we also apply additional methods such as staining and microscopy to verify the performance of waveform-based image-guided cell sorting.

Fig 3.6 shows an example of how the temporal waveform carries features about particle size and how we can use the waveform features to distinguish 15μm and 7μm diameter beads. When there is no object in the microfluidic channel, the scanning Bessel Gaussian beam transmits through the slit and the PMT shows a periodic background signal, caused by any imperfections or dust particles in the COC microfluidic chip intersected by the laser beam. Since these features are still, they appear to be periodic in each scan and can be subtracted by software. When a cell or bead travels through the optical interrogation area, it creates an instantaneous change in the PMT output signal on top of the background. The PMT waveforms in Figs. 3.6(a-i) and 3.6(b-i) show an envelope with a series of spikes. Each spike represents a single scan spanning a duration of 5μs, and the width of the spike is proportional to the size of the bead along the scanning (y-) direction. On the other hand, the width of the overall signal envelope is proportional to the dimension of the bead in the flow direction after correction of the effect of the flow speed. Based on this argument, we develop the following sorting criterion that is equivalent to the particle size:

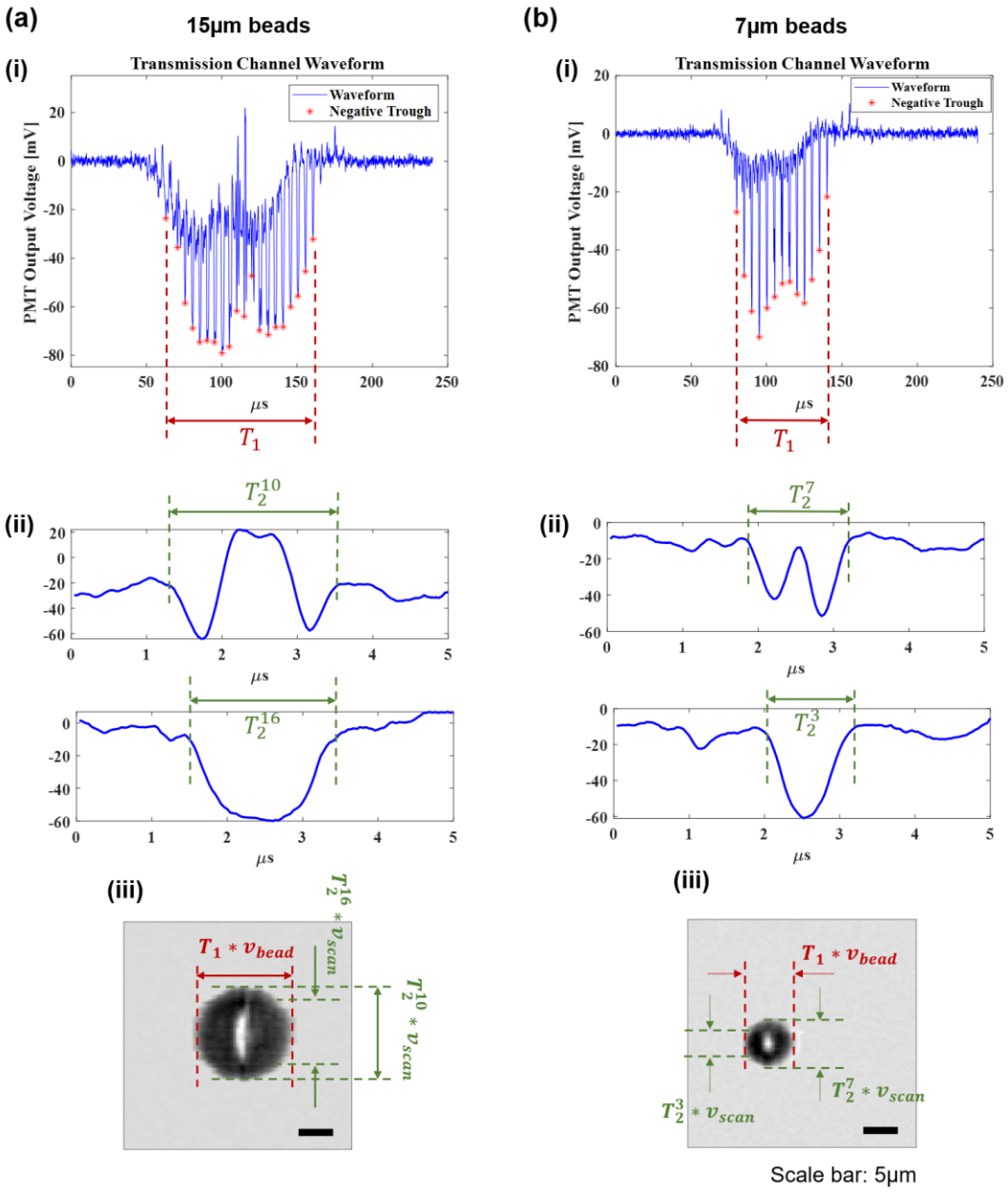

Figure 3.6. Transmission PMT signals for 15μm and 7μm beads and reconstructed images. Scale bar: 5μm. (i) The overall signals. Each "*" represents the peak of each scan. The product of the bead speed v_{bead} and the width of the overall envelope T_1 produces the bead dimension along the flow direction. (ii) Detailed waveforms for a single 5μs AOD scan. At each specific z-position, the dimension of the bead along the scanning direction is $T_2 * v_{scan}$ where $v_{scan} = 8m/s$ is the beam scanning speed. (iii) Reconstructed transmission images of a 15 μm and 7 μm bead. The relations between the temporal waveforms and the image features are also indicated in the figures.

We find the time interval between the first negative peak and the last negative peak T_1, which corresponds to the duration when the bead crosses the optical interrogation zone defined by the width of the slit in the spatial mask. The bead length L along the flow direction equals $T_1 * v_{bead}$, where v_{bead} is bead traveling speed. We then analyze the detailed waveform of each 5μs scan (labelled by "*" in the envelope waveform) to find the bead dimension in the scanning direction. Figs 3.6(a-ii) and (b-ii) show the detailed waveform of each 5μs scan at a given z position. By slicing the object into N sections along the z-position, the object width at the nth section can be represented as $T_2^n * v_{scan}$ with n being the index of the z-position and v_{scan} is the beam scanning speed ($v_{scan} = 8m/s$). Fig 3.6(a-ii) shows two (10th and 16th) of such scans for a 15μm bead. The 10th scan gives the largest value of $T_2^n * v_{scan}$, indicating the widest part (i.e. diameter) of the bead. Similar characteristics can be found in the waveform of 7μm beads. The above example demonstrates how one can relate the temporal waveform features to the geometric features of a travelling object such as size, shape, aspect ratio, etc.

3 Experimental Results

3.1 Sorting of 10 and 15μm beads

To validate the sorting algorithm described above, a sorting experiment was done using 7μm, 10μm and 15μm beads. The histogram of $(T_1 * v_{bead}) * (T_2 * v_{scan})$ is shown in Fig. 3.7(b). To evaluate sorting performance, we sorted 10μm beads from a 1:1 mixture of 7μm and 10μm beads, as well as 15μm beads from a 1:1 mixture of 7μm and 15μm beads. The sorted beads were imaged using a microscope to verify the sorting accuracy. The first experiment demonstrated a sorting purity of 97%, verified by 233 microscope images; and the second experiment demonstrated 100% sorting purity, verified by 173 microscope images.

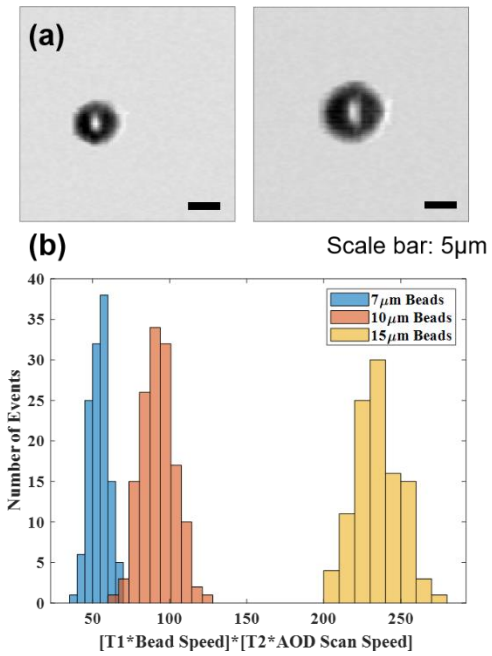

Figure 3.7. Images and histograms of polystyrene beads generated by the Bessel-Gaussian beam image-guided cell sorter. (a) Transmission images of polystyrene beads with 7μm (left) and 10μm (right) diameter. Scale bar: 5μm. (b) Histogram of $(T_1 * v_{bead}) * (T_2 * v_{scan})$ for 7μm, 10μm and 15μm beads.

3.2 Label-free sorting of leukemia cells

Blood cancers such as acute myeloid leukemia (AML) are estimated to account for 9.9% of the 1.8 million new cancer cases diagnosed in 2020 [23]. Leukemia, lymphoma and myeloma are expected to account for 9.4% of all cancer deaths in 2020 [79].

Acute myeloid leukemia is derived from the myeloid line of blood cells and is characterized by its rapid and unchecked growth of abnormal cells in the bone marrow that interferes with normal blood cell production. Diagnosis usually occurs via bone marrow aspiration or antibody-specific blood tests [80]. However, these require costly panels and tedious procedures. An image-guided cell sorter enables the identification and subsequent sorting of AML cells without any antibody or fluorescent labeling, aiding early detection and eliminating the need for costly reagents and tedious laboratory procedures.

In a proof-of-concept experiment, patient-derived SKNO1 acute myeloid leukemia (AML) cells were cultured in cell culture media (90% RPMI + 8% FBS + 1% penicillin + 1% streptomycin) at 37℃ with 5% CO_2. The SKNO1 cells were spiked into white blood cells from healthy donors (San Diego Blood Bank, 3636 Gateway Center Ave Suite 100, San Diego). A number of feature parameters were extracted from the transmission waveform of these cells, which are intuitively related to cell area, perimeter, granularity, roughness, contrast, and texture. The most distinguishing features between SKNO1 cells and white blood cells were determined to be $T_1 * v_{cell}$ and the number of positive peaks of the waveform. The former is related to cell size and the latter to intracellular granularity. To demonstrate image-guided label-free cell sorting, a 2D plot of these parameters was generated and the appropriate gating parameters were chosen to sort SKNO1 cells from healthy white blood cells in a ratio of 1:50. To evaluate the cell sorting, Wright-Giemsa staining was performed. The full details for the staining procedure can be found in the supplementary material. The sorted cells were collected in a tube and deposited on a polyester transparent membrane filter (1300019, Sterlitech). Wright-Giemsa staining was performed and the stained cells were imaged using brightfield microscopy. A total of 124 SKNO1 cells were imaged from a total of 128 cells found on the membrane, giving rise to a sorting purity of 97%. Given the initial population of 2% SKNO1 cells, the sorting has enriched the sample by 1600 times.

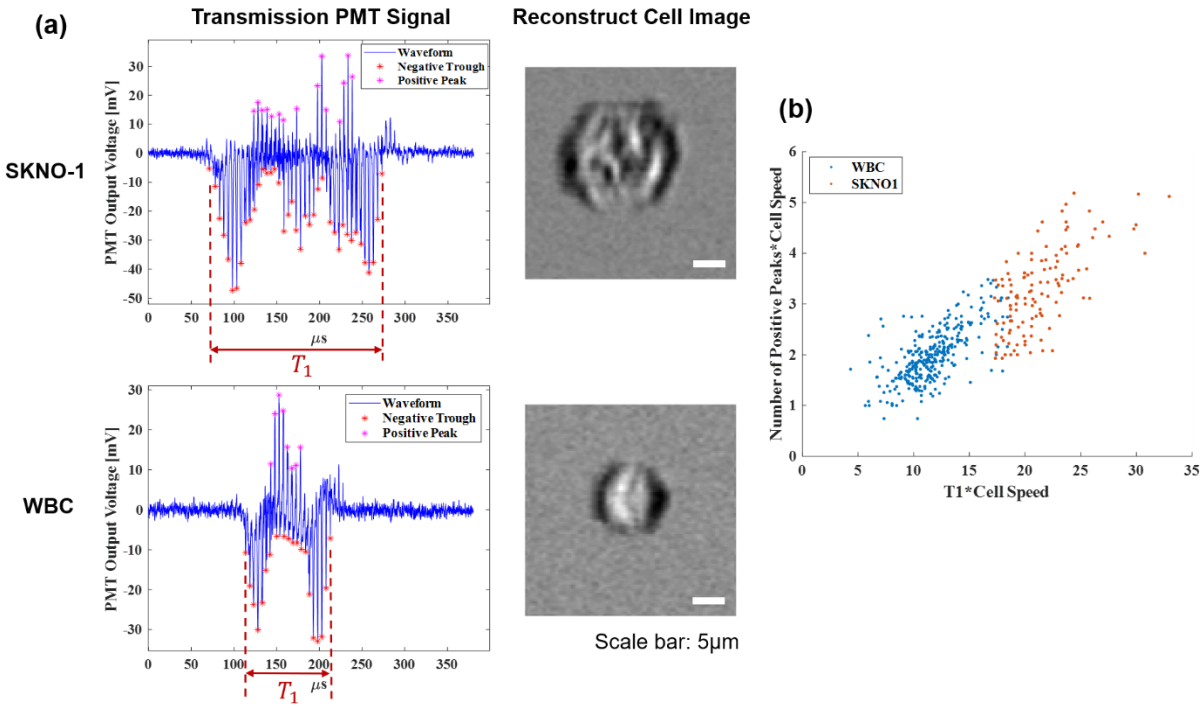

Figure 3.8. (a) Transmission PMT signals and images for SKNO-1 and WBC generated by the Bessel-Gaussian beam image-guided cell sorter. Scale bar: 5μm. (b) Distribution plots using these two parameters: $T_1 * v_{cell}$ and $N * v_{cell}$ where N is the number of positive peaks in the PMT waveform. Multiplication of cell speed to both parameters remove feature distortions due to cell speed variations.

3.3 Label-Free Sorting of *Scenedesmus sp.*

Algae are a group of photosynthetic, eukaryotic organisms that can be found in oceans, waterways, lakes, and soils all over the world. Algae are commonly used to monitor environmental changes and have a number of industrial uses, including the production of biodiesel, ceramic products, glass products; in wastewater and oil spill cleanup; and in the biotechnology field as anticoagulant, antiviral and antitumor agents [81-84]. Despite their usefulness, little is known regarding the majority of these algae, with the estimated number of microalgae species exceeding one million [85]. In comparison, the best algae culture collections often contain only a few thousand species [86]. Isolation of microalgae species from the environment is a useful and necessary approach to understanding these organisms and

uncovering potential technological solutions. Traditionally, these organisms are isolated by hand using micropipettes or capillary tubes, or by fluorescence-activated cell sorting, and are subsequently cultured [87]. However, the throughput and usefulness of these approaches are limited, as microalgae and other microorganisms experience complex relationships with surrounding organisms that affect algae phenotype.

Scenedesmus sp. is one of the most common freshwater green algae. These colonial, non-motile algae have been researched for its high biomass productivity and its efficiency at capturing CO_2 [88]. *Scenedesmus* is capable of producing many types of biofuels and has been most extensively studied for biodiesel production. As there are over seventy taxonomically accepted species of *Scenedesmus*, including some with unique properties that only exist in local populations, the high-throughput identification and sorting of these algae from field-collected samples could unlock new opportunities [88].

As a proof-of-concept sorting experiment, *Scenedesmus* (Carolina Biological Supply, 152510) were spiked into field-collected microorganisms (Miramar Lake, San Diego, California) in a ratio of 1:5. The sample was run through a 35μm filter to remove clumps and large particles. The distinguishing feature of Scenedesmus from the other microorganisms was $T_1 * v_{algae}$, which intuitively relates to size. A histogram with these parameters was generated and the appropriate portion was gated. The sorted samples were collected into tubes and visualized using brightfield microscopy. From a total of 253 sorted cells verified by microscope, 248 of them were Scenedesmus and 5 were other microorganisms, resulting in a sorting purity of 98%.

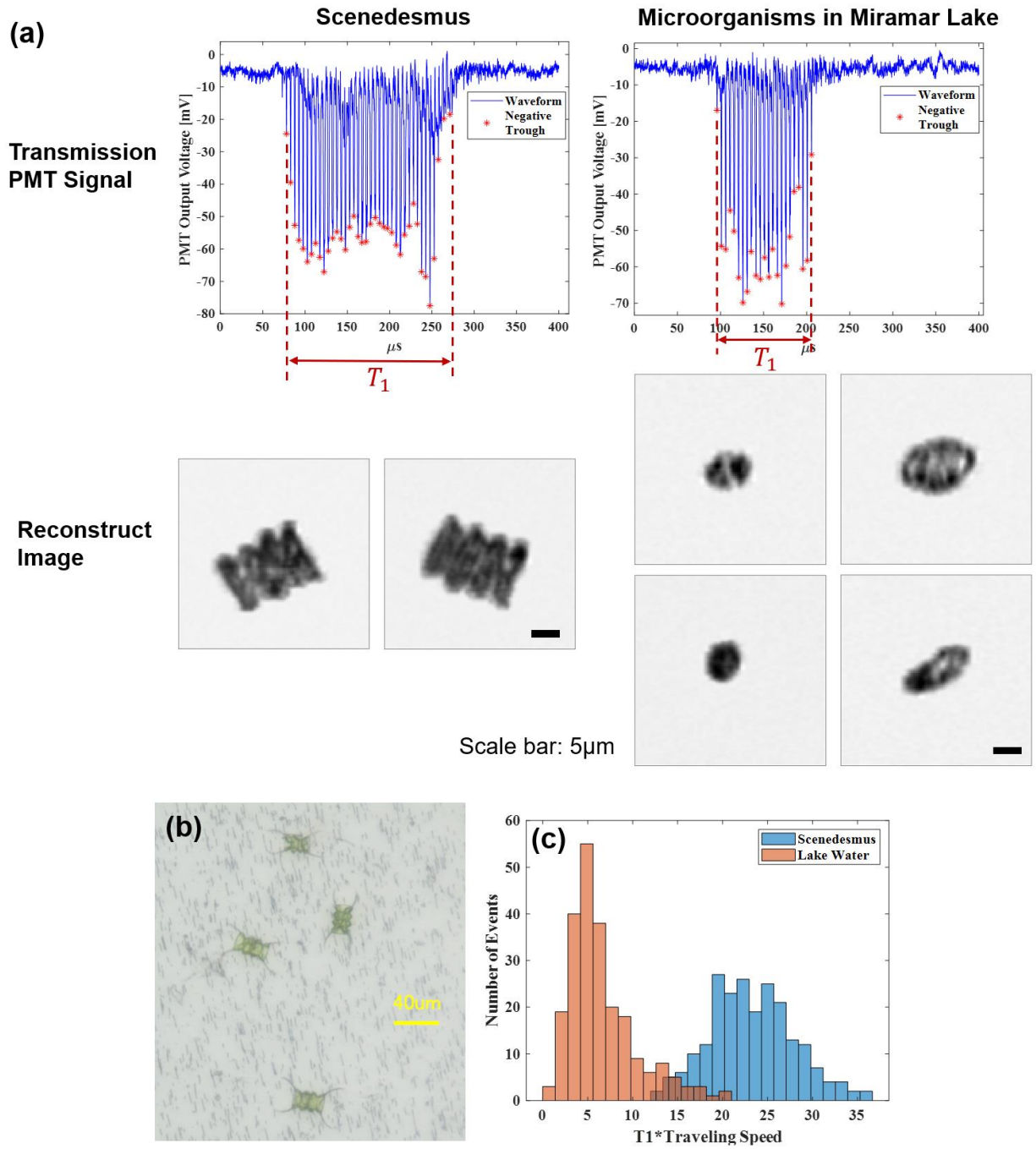

Figure 3.9. (a) Transmission channel waveforms and reconstructed images of Scenedesmus and microorganisms in Miramar Lake water. Scale bar: 5μm. (b) Optical microscope images of Scenedesmus being sorted on membrane filter. (c) Histogram of $T_1 * v_{algae}$ for Scenedesmus and other microorganisms in lake water.

Acknowledgements

Chapter 3, in full, is a reprint of the material as it appears in Applied Physics Letter (APL) Photonics. Chen, Xinyu; Waller, Lauren; Chen, Jiajie; Tang, Rui; Zhang, Zunming; Gagne, Ivan; Gutierrez, Bien; Cho, Sung-Hwan; Tseng, Chi-Yang; Lian Ian Y; Lo, Yu-Hwa, AIP Publishing, 2021. The dissertation author was the primary researcher and author of this paper.

1 Background

We have illustrated the importance of detecting cell images in a label-free manner in the previous chapter. Current imaging flow cytometers, including the commercialized ones like Amnis® ImageStream®X and the IFC with 3D imaging capabilities are able to provide 2D transmission (brightfield) images and 2D/3D side scattering images. Forward scattering is also one of the most important parameters in flow cytometry analysis. However, due to technical challenges, flow cytometers that can produce 2D or 3D forward scattering images are still under development. Here we propose a method to solve this problem, leveraging fast laser scanning, needle-shaped beam and PMT array detector.

Though an ideal Bessel beam can theoretically retain its intensity profile after an infinite travel distance in space, the sidelobes can still complicate the computation or optical setup. As a result, people developed needle-shaped beam (NB), which is capable of maintaining high transverse resolution over a large depth-of-focus, also featured by the removal of sidelobes [89]. Zhao *et.al.* developed a spatially multiplexed phase pattern that creates many axially closely spaced foci as a universal platform for customizing various NBs, allowing flexible manipulations of beam length and diameter [90]. The phase mask was created on a diffractive optical element (DOE) that was fabricated on a fused silica wafer via several rounds of lithography. The DOE is composed of 1024×1024 10 μm pixels (Fig. 4.1 (a-c)), with a beam length of 40um and 9 foci (Fig. 4.1 (d)).

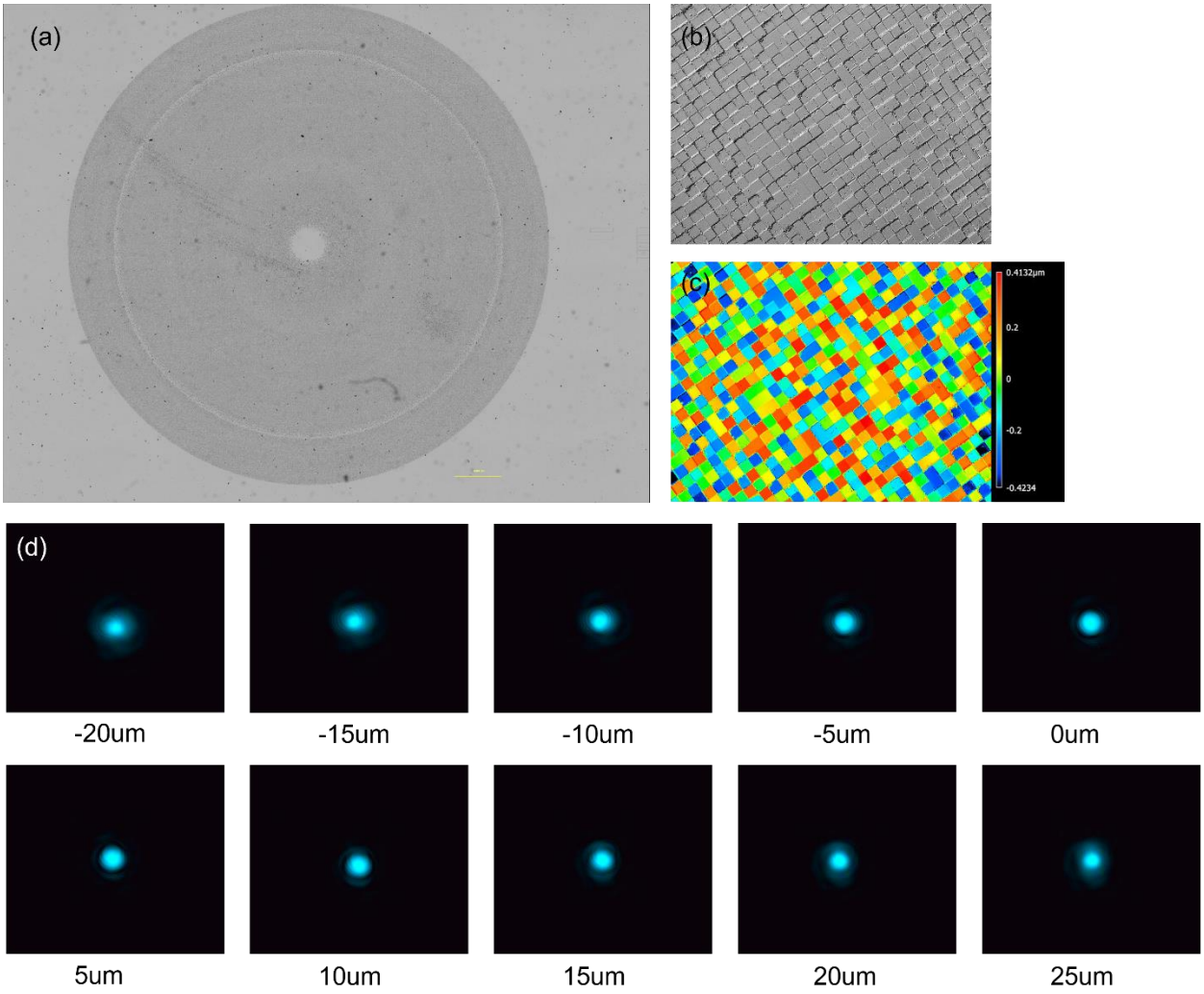

Figure 4.1. (a) Laser microscope (VK-X3000, Keyence) images of the diffractive optical element. (b) One enlarged area of (a). (c) height profile of (b). (c) Laser beam profile at the focal plane of the imaging system.

2 Methods

2.1 Design of the Imaging System

The optical system design is shown in Fig. 4.2 (a). The Gaussian beam output from a 488nm diode laser with a beam diameter of 0.7mm is modulated by an acousto-optic deflector (488-A, CASTECH). The acoustic transducer deflects the beam to different angles along the y- (scanning) direction at a frequency of 200kHz. The laser beam is then expanded to a diameter of 3mm and illuminates on the DOE shown in Fig. 4.1. The needle-shaped beam is formed at the

focal plane of a 20X objective lens (378-804-3, Mitutoyo). The position of the AOD is conjugated with the DOE. An LED is also coupled into the optical path as a light source during sample alignment. Forward scattering signals, as well as laser transmission light are collected by a 50X objective lens (378-805-3, Mitutoyo). However, a black square with 8mm width and 4mm height blocks all the transmission light, only allowing forward scattering light passing through.

The three-dimensional field of view, which is 40μm (scanning, or x-direction) by 40μm (flow, or y-direction) by 40μm (laser propagating, or z-direction), is artificially divided to eight x-y planes with roughly equal intervals. As shown in Fig. 4.2 (a), scattering signals from the first x-y plane are collected by the 50X objective lens and then focused by a 150mm lens. A micro-mirror is placed right at the focal point. The mirror is tilted at a 45-degree angle to the optical axis such that the scattering light beam is reflected down to the optics table. The scattering signals from the second x-y plane are also focused by the 150mm lens, with a focal point that is behind the focal point corresponding to the first x-y plane. Though part of the light beam corresponding to the second x-y plane will be intersected by the first micro-mirror, due to the relatively small size of the mirror, most of the beam will still reach the geometrically determined focal point, where a second micro-mirror is placed. As a result, it is not hard to imagine that a series of micro-mirrors with same geometries and intervals, with each of them placed at the focal point corresponding to one artificial object plane, will split the mixed forward scattering signals from different depth to spatially separated paths, which can be quantified by different detectors. Here we use a detector array composed of eight PMTs (H9530-20, Hamamatsu), and the intervals between focal points are designed to match the pitches of the PMTs.

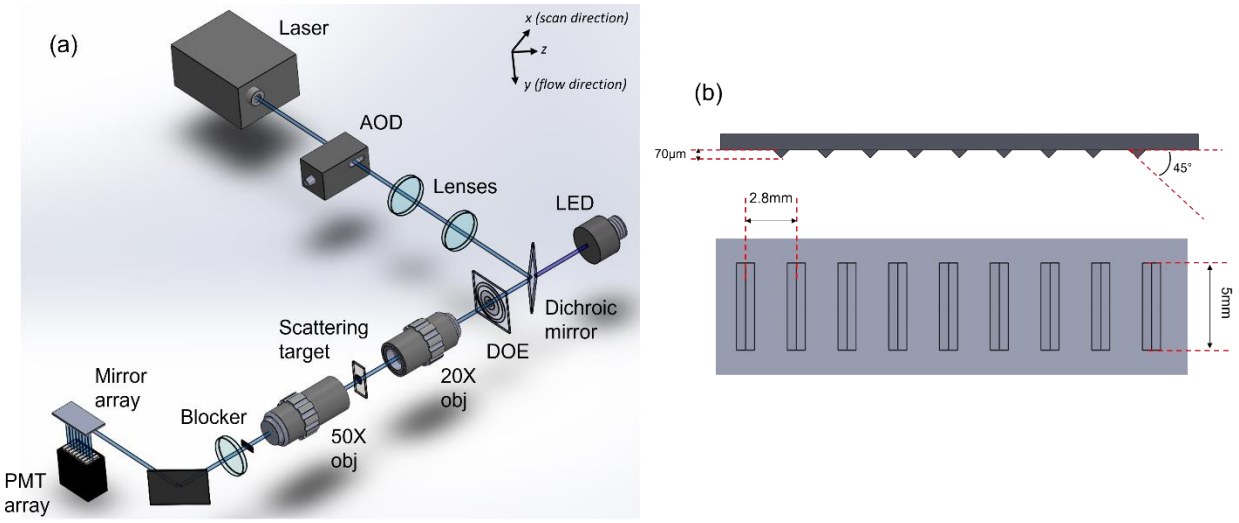

Figure 4.2. (a) Design of the imaging system. DOE: diffractive optical element. (b) Design of the micro-mirror array

2.2 Devices Fabrication

To make the fabrication process feasible, the micro-mirror array is designed to be an array of prism, each of which has a length of 5mm, aligned to the x-direction, and a height of 70μm. The prism array is made by layer-by-layer deposition of negative-tone resins on a silicon wafer (Photonic Pro GT2, Nanoscribe), followed by developing in propylene glycol methyl ether acetate (PGMEA) for 10min and rinsing in isopropyl alcohol (IPA). To make the surface reflective, a 125nm aluminum layer was sputtered on the array (Discovery 18, Denton). The layer is formed under 80 sccm Argon air flow, 5mT chamber pressure, 100W DC power and a deposition time of 5min. The scattering target (Fig 4.3 (b)) is made of a similar process by depositing resins on a transparent substrate.

3 Results

3.1 Channel crosstalk quantification

As shown in Fig 4.3 (a), the forward scattering signals from any focal planes (FPs), except for the first FP, will be partially intersected by the previous mirror, which means that even

if the scattering center is only located at the second FP, the first PMT will also receive some signals. We call this phenomenon “crosstalk”. The situation of other FPs can be speculated accordingly. The crosstalk between all the PMTs within the 40μm range is simulated by moving a scattering center along z axis (Fig. 4.3 (c)). We can observe that when PMT j (1<j<8) reaches its maximum, PMT j-1 and PMT j+1 also have signal output. The reasons can be related to the relatively large size of the needle-shaped beam (4 μm $1/e^2$ diameter), which leads to the excitation of off-axis scattering centers, as well as the variations of scattering angles from the scattering center.

A test sample which serves as a 3D scattering object was fabricated as described in the previous chapter. The sample has eight steps forming a staircase-like structure, with a step size of 2.5μm. Several 1μm x 1μm x 1μm bumps are placed on each tier, including the ground floor, which will generate strong scattering signal under laser illumination. We fixed the laser position on one of the bumps and move the test sample along z-axis with an incremental of 1μm. The output intensity of each PMT was recorded and plotted against the z position (Fig 4.3 (d)).

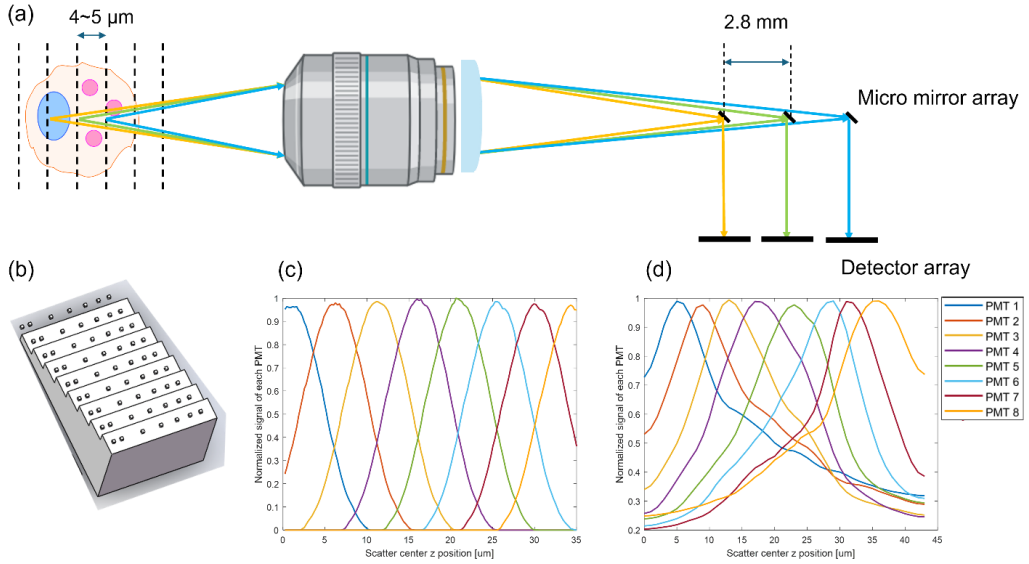

Figure 4.3. (a) Schematic of 3D forward scattering detection working principles and the reasons for crosstalk. (b) Scattering target test sample. (c) Simulated crosstalk (Zemax, Ansys). (d) Measured crosstalk.

3.2 Forward Scattering image reconstruction

The test sample in Fig 4.3 (b) was mounted on a xyz stage, placed within the focal length of the DOE, with the step edges aligned with the scanning direction of the laser beam. We manually moved the sample along flow direction with a distance corresponding to three tiers and recorded the outputs of all the PMTs. For each PMT, the temporal waveforms were reconstructed to a 3D image using the algorithm described in Chapter 2 (Fig 4.4 (a)). The strong signals with line structures come from the step edges. We can observe that signals from tier 1 reach their highest at PMT#5. Signals from tier 2 have similar intensities at PMT#4 and PMT#5, and signals from tier 3 reach their highest at PMT#4.

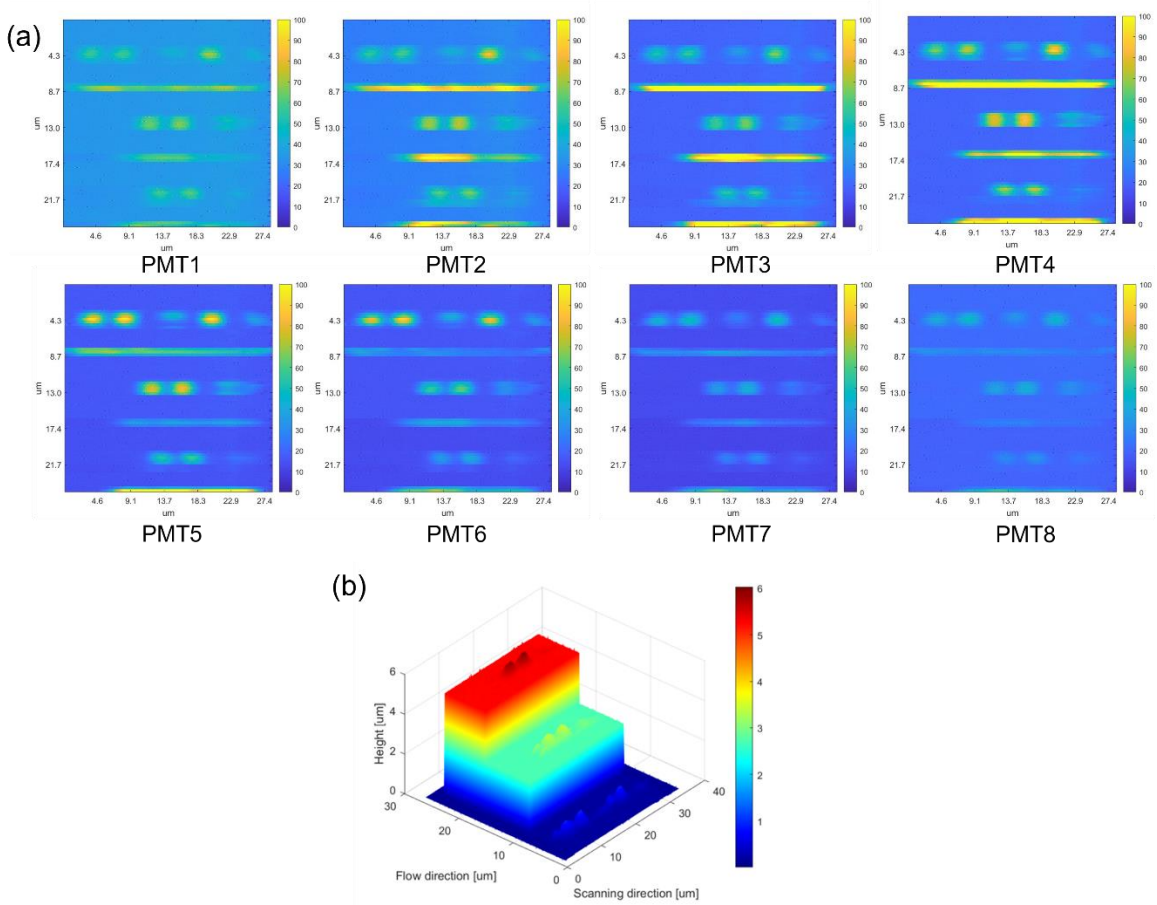

Figure 4.4. (a) Reconstructed 2D images of the scattering target test sample using the output signals from each PMT. (b) Reconstructed 3D image of the scattering target, considering the steps.

For the images in Fig 4.4 (a), we extracted the part of tier 1 at PMT#5, the average of tier 2 at PMT#4 and PMT#5, and tier 3 at PMT#4. Since the relationship between PMT output and the positions of object planes is known, we can reconstruct the 3D forward scattering images of the test sample, which is shown in Fig 4.4 (b).

Acknowledgements

Chapter 4, in part is currently being prepared for submission for publication of the material. Chen, Xinyu; Zhou, Minhong; Zhou, Ziqi; Tang, Rui; Zhang, Zunming; Lo, Yu-Hwa. The dissertation author was the primary researcher and author of this material.

REFERENCES

[1] McKinnon, K.M., 2018. Flow cytometry: an overview. Current protocols in immunology, 120(1), pp.5-1.

[2] Adan, A., Alizada, G., Kiraz, Y., Baran, Y. and Nalbant, A., 2017. Flow cytometry: basic principles and applications. Critical reviews in biotechnology, 37(2), pp.163-176.

[3] Wlodkowic, D., Skommer, J. and Darzynkiewicz, Z., 2011. Rapid quantification of cell viability and apoptosis in B-cell lymphoma cultures using cyanine SYTO probes. Mammalian Cell Viability: Methods and Protocols, pp.81-89.

[4] Han, Y. and Lo, Y.H., 2015. Imaging cells in flow cytometer using spatial-temporal transformation. Scientific reports, 5(1), p.13267.

[5] Blasi, T., Hennig, H., Summers, H.D., Theis, F.J., Cerveira, J., Patterson, J.O., Davies, D., Filby, A., Carpenter, A.E. and Rees, P., 2016. Label-free cell cycle analysis for high-throughput imaging flow cytometry. Nature communications, 7(1), p.10256.

[6] Fuhrmann, A., Banisadr, A., Beri, P., Tlsty, T.D. and Engler, A.J., 2017. Metastatic state of cancer cells may be indicated by adhesion strength. Biophysical Journal, 112(4), pp.736-745.

[7] Clarkson, B.D., Héninger, E., Harris, M.G., Lee, J., Sandor, M. and Fabry, Z., 2012. Innate-adaptive crosstalk: how dendritic cells shape immune responses in the CNS. Current Topics in Innate Immunity II, pp.309-333.

[8] Marques, E., Peltola, T., Kaski, S. and Klefström, J., 2018. Phenotype-driven identification of epithelial signalling clusters. Scientific Reports, 8(1), p.4034.

[9] Harris, L.K. and Theriot, J.A., 2016. Relative rates of surface and volume synthesis set bacterial cell size. Cell, 165(6), pp.1479-1492.

[10] Novák, B., Heldt, F.S. and Tyson, J.J., 2018. Genome stability during cell proliferation: A systems analysis of the molecular mechanisms controlling progression through the eukaryotic cell cycle. Current opinion in systems biology, 9, pp.22-31.

[11] Shaffer, S.M., Dunagin, M.C., Torborg, S.R., Torre, E.A., Emert, B., Krepler, C., Beqiri, M., Sproesser, K., Brafford, P.A., Xiao, M. and Eggan, E., 2017. Rare cell variability and drug-induced reprogramming as a mode of cancer drug resistance. Nature, 546(7658), pp.431-435.

[12] Yu, M., Stott, S., Toner, M., Maheswaran, S. and Haber, D.A., 2011. Circulating tumor cells: approaches to isolation and characterization. Journal of Cell Biology, 192(3), pp.373-382.

[13] Fulwyler, M.J., Glascock, R.B., Hiebert, R.D. and Johnson, N.M., 1969. Device which separates minute particles according to electronically sensed volume. Review of Scientific Instruments, 40(1), pp.42-48.

[14] Bonner, W.A., Hulett, H.R., Sweet, R.G. and Herzenberg, L.A., 1972. Fluorescence activated cell sorting. Review of Scientific Instruments, 43(3), pp.404-409.

[15] Gale, B.K., Jafek, A.R., Lambert, C.J., Goenner, B.L., Moghimifam, H., Nze, U.C. and Kamarapu, S.K., 2018. A review of current methods in microfluidic device fabrication and future commercialization prospects. Inventions, 3(3), p.60.

[16] Godin, J., Chen, C.H., Cho, S.H., Qiao, W., Tsai, F. and Lo, Y.H., 2008. Microfluidics and photonics for Bio-System-on-a-Chip: A review of advancements in technology towards a microfluidic flow cytometry chip. Journal of biophotonics, 1(5), pp.355-376.

[17] Cho, S.H., Godin, J.M., Chen, C.H., Qiao, W., Lee, H. and Lo, Y.H., 2010. Recent advancements in optofluidic flow cytometer. Biomicrofluidics, 4(4).

[18] Hawkins, A.R. and Schmidt, H., 2010. Handbook of optofluidics. CRC press.

[19] Chiu, Y.J., Cho, S.H., Mei, Z., Lien, V., Wu, T.F. and Lo, Y.H., 2013. Universally applicable three-dimensional hydrodynamic microfluidic flow focusing. Lab on a Chip, 13(9), pp.1803-1809.

[20] Zhao, Y., Li, Q. and Hu, X., 2018. Universally applicable three-dimensional hydrodynamic focusing in a single-layer channel for single cell analysis. Analytical methods, 10(28), pp.3489-3497.

[21] Fu, L.M., Yang, R.J., Lin, C.H., Pan, Y.J. and Lee, G.B., 2004. Electrokinetically driven micro flow cytometers with integrated fiber optics for on-line cell/particle detection. Analytica Chimica Acta, 507(1), pp.163-169.

[22] Doh, I. and Cho, Y.H., 2005. A continuous cell separation chip using hydrodynamic dielectrophoresis (DEP) process. Sensors and Actuators A: Physical, 121(1), pp.59-65.

[23] Adams, J.D., Kim, U. and Soh, H.T., 2008. Multitarget magnetic activated cell sorter. Proceedings of the National Academy of Sciences, 105(47), pp.18165-18170.

[24] Bang, H., Chung, C., Kim, J.K., Kim, S.H., Chung, S., Park, J., Lee, W.G., Yun, H., Lee, J., Cho, K. and Han, D.C., 2006. Microfabricated fluorescence-activated cell sorter through hydrodynamic flow manipulation. Microsystem Technologies, 12, pp.746-753.

[25] Chen, C.H., Cho, S.H., Tsai, F., Erten, A. and Lo, Y.H., 2009. Microfluidic cell sorter with integrated piezoelectric actuator. Biomedical microdevices, 11, pp.1223-1231.

[26] Cho, S.H., Chen, C.H., Tsai, F.S., Godin, J.M. and Lo, Y.H., 2010. Human mammalian cell sorting using a highly integrated micro-fabricated fluorescence-activated cell sorter (μFACS). Lab on a Chip, 10(12), pp.1567-1573.

[27] [Online]. Available: https://nanocellect.com/

[28] Wu, T.H., Chen, Y., Park, S.Y., Hong, J., Teslaa, T., Zhong, J.F., Di Carlo, D., Teitell, M.A. and Chiou, P.Y., 2012. Pulsed laser triggered high speed microfluidic fluorescence activated cell sorter. Lab on a Chip, 12(7), pp.1378-1383.

[29] Chen, Y., Wu, T.H., Kung, Y.C., Teitell, M.A. and Chiou, P.Y., 2013. 3D pulsed laser-triggered high-speed microfluidic fluorescence-activated cell sorter. Analyst, 138(24), pp.7308-7315.

[30] Chen, Y., Chung, A.J., Wu, T.H., Teitell, M.A., Di Carlo, D. and Chiou, P.Y., 2014, April. Pulsed laser activated cell sorting with three dimensional sheathless inertial focusing. In The 9th IEEE International Conference on Nano/Micro Engineered and Molecular Systems (NEMS) (pp. 315-318). IEEE.

[31] Pozarowski, P., Holden, E. and Darzynkiewicz, Z., 2006. Laser scanning cytometry: principles and applications. Cell Imaging Techniques: Methods and Protocols, pp.165-192.

[32] Henriksen, M., 2010. Quantitative imaging cytometry: instrumentation of choice for automated cellular and tissue analysis.

[33] Han, Y., Gu, Y., Zhang, A.C. and Lo, Y.H., 2016. Imaging technologies for flow cytometry. Lab on a Chip, 16(24), pp.4639-4647.

[34] George, T.C., Basiji, D.A., Hall, B.E., Lynch, D.H., Ortyn, W.E., Perry, D.J., Seo, M.J., Zimmerman, C.A. and Morrissey, P.J., 2004. Distinguishing modes of cell death using the ImageStream® multispectral imaging flow cytometer. Cytometry Part A: the journal of the International Society for Analytical Cytology, 59(2), pp.237-245.

[35] Goda, K., Filby, A. and Nitta, N., 2019. In flow cytometry, image is everything. Cytometry Part A, 95(5), pp.475-477.

[36] George, T.C., Basiji, D.A., Hall, B.E., Lynch, D.H., Ortyn, W.E., Perry, D.J., Seo, M.J., Zimmerman, C.A. and Morrissey, P.J., 2004. Distinguishing modes of cell death using the ImageStream® multispectral imaging flow cytometer. Cytometry Part A: the journal of the International Society for Analytical Cytology, 59(2), pp.237-245.

[37] George, T.C., Fanning, S.L., Fitzgeral-Bocarsly, P., Medeiros, R.B., Highfill, S., Shimizu, Y., Hall, B.E., Frost, K., Basiji, D., Ortyn, W.E. and Morrissey, P.J., 2006. Quantitative measurement of nuclear translocation events using similarity analysis of multispectral cellular images obtained in flow. Journal of immunological methods, 311(1-2), pp.117-129.

[38] Beum, P.V., Lindorfer, M.A., Hall, B.E., George, T.C., Frost, K., Morrissey, P.J. and Taylor, R.P., 2006. Quantitative analysis of protein co-localization on B cells opsonized with rituximab and complement using the ImageStream multispectral imaging flow cytometer. Journal of immunological methods, 317(1-2), pp.90-99.

[39] Zuba-Surma, E.K., Kucia, M., Abdel-Latif, A., Dawn, B., Hall, B., Singh, R., Lillard Jr, J.W. and Ratajczak, M.Z., 2008. Morphological characterization of very small embryonic-like stem cells (VSELs) by ImageStream system analysis. Journal of cellular and molecular medicine, 12(1), pp.292-303.

[40] Goda, K., Tsia, K.K. and Jalali, B., 2009. Serial time-encoded amplified imaging for real-time observation of fast dynamic phenomena. Nature, 458(7242), pp.1145-1149.

[41] Goda, K., Ayazi, A., Gossett, D.R., Sadasivam, J., Lonappan, C.K., Sollier, E., Fard, A.M., Hur, S.C., Adam, J., Murray, C. and Wang, C., 2012. High-throughput single-microparticle imaging flow analyzer. Proceedings of the National Academy of Sciences, 109(29), pp.11630-11635.

[42] Diebold, E.D., Buckley, B.W., Gossett, D.R. and Jalali, B., 2013. Digitally synthesized beat frequency multiplexing for sub-millisecond fluorescence microscopy. Nature Photonics, 7(10), pp.806-810.

[43] Han, Y. and Lo, Y.H., 2016, March. Imaging flow cytometer using computation and spatially coded filter. In High-Speed Biomedical Imaging and Spectroscopy: Toward Big Data Instrumentation and Management (Vol. 9720, pp. 126-136). SPIE.

[44] Wu, J., Li, J. and Chan, R.K., 2013. A light sheet based high throughput 3D-imaging flow cytometer for phytoplankton analysis. Optics express, 21(12), pp.14474-14480.

[45] Quint, S., Christ, A.F., Guckenberger, A., Himbert, S., Kaestner, L., Gekle, S. and Wagner, C., 2017. 3D tomography of cells in micro-channels. Applied Physics Letters, 111(10).

[46] Sung, Y., Lue, N., Hamza, B., Martel, J., Irimia, D., Dasari, R.R., Choi, W., Yaqoob, Z. and So, P., 2014. Three-dimensional holographic refractive-index measurement of continuously flowing cells in a microfluidic channel. Physical review applied, 1(1), p.014002.

[47] Merola, F., Memmolo, P., Miccio, L., Savoia, R., Mugnano, M., Fontana, A., D'ippolito, G., Sardo, A., Iolascon, A., Gambale, A. and Ferraro, P., 2017. Tomographic flow cytometry by digital holography. Light: Science & Applications, 6(4), pp.e16241-e16241.

[48] Martin, C., Li, T., Hegarty, E., Zhao, P., Mondal, S. and Ben-Yakar, A., 2018. Line excitation array detection fluorescence microscopy at 0.8 million frames per second. Nature Communications, 9(1), p.4499.

[49] Han, Y., Tang, R., Gu, Y., Zhang, A.C., Cai, W., Castor, V., Cho, S.H., Alaynick, W. and Lo, Y.H., 2019. Cameraless high-throughput three-dimensional imaging flow cytometry. Optica, 6(10), pp.1297-1304.

[50] Tang, R., Zhang, Z., Chen, X., Waller, L., Zhang, A.C., Chen, J., Han, Y., An, C., Cho, S.H. and Lo, Y.H., 2020. 3D side-scattering imaging flow cytometer and convolutional neural network for label-free cell analysis. APL Photonics, 5(12).

[51] Zhang, Z., Chen, X., Tang, R., Zhu, Y., Guo, H., Qu, Y., Xie, P., Lian, I.Y., Wang, Y. and Lo, Y.H., 2023. Interpretable unsupervised learning enables accurate clustering with high-throughput imaging flow cytometry. Scientific Reports, 13(1), p.20533.

[52] Chattopadhyay, P.K., Gierahn, T.M., Roederer, M. and Love, J.C., 2014. Single-cell technologies for monitoring immune systems. Nature immunology, 15(2), pp.128-135.

[53] Jiang, Y., Lei, C., Yasumoto, A., Kobayashi, H., Aisaka, Y., Ito, T., Guo, B., Nitta, N., Kutsuna, N., Ozeki, Y. and Nakagawa, A., 2017. Label-free detection of aggregated platelets in blood by machine-learning-aided optofluidic time-stretch microscopy. Lab on a Chip, 17(14), pp.2426-2434.

[54] von Erlach, T.C., Bertazzo, S., Wozniak, M.A., Horejs, C.M., Maynard, S.A., Attwood, S., Robinson, B.K., Autefage, H., Kallepitis, C., del Río Hernández, A. and Chen, C.S., 2018. Cell-geometry-dependent changes in plasma membrane order direct stem cell signalling and fate. Nature materials, 17(3), pp.237-242.

[55] Boutros, M., Heigwer, F. and Laufer, C., 2015. Microscopy-based high-content screening. Cell, 163(6), pp.1314-1325.

[56] Caicedo, J.C., Cooper, S., Heigwer, F., Warchal, S., Qiu, P., Molnar, C., Vasilevich, A.S., Barry, J.D., Bansal, H.S., Kraus, O. and Wawer, M., 2017. Data-analysis strategies for image-based cell profiling. Nature methods, 14(9), pp.849-863.

[59] Gu, Y., Zhang, A.C., Han, Y., Li, J., Chen, C. and Lo, Y.H., 2019. Machine learning based real-time image-guided cell sorting and classification. Cytometry Part A, 95(5), pp.499-509.

[58] Nitta, N., Sugimura, T., Isozaki, A., Mikami, H., Hiraki, K., Sakuma, S., Iino, T., Arai, F., Endo, T., Fujiwaki, Y. and Fukuzawa, H., 2018. Intelligent image-activated cell sorting. Cell, 175(1), pp.266-276.

[59] Goldman, S.L., MacKay, M., Afshinnekoo, E., Melnick, A.M., Wu, S. and Mason, C.E., 2019. The impact of heterogeneity on single-cell sequencing. Frontiers in genetics, 10, p.8.

[60] Hasle, N., Cooke, A., Srivatsan, S., Huang, H., Stephany, J.J., Krieger, Z., Jackson, D., Tang, W., Pendyala, S., Monnat Jr, R.J. and Trapnell, C., 2020. High-throughput, microscope-based sorting to dissect cellular heterogeneity. Molecular Systems Biology, 16(6), p.e9442.

[61] Hochstetter, A., Vernekar, R., Austin, R.H., Becker, H., Beech, J.P., Fedosov, D.A., Gompper, G., Kim, S.C., Smith, J.T., Stolovitzky, G. and Tegenfeldt, J.O., 2020. Deterministic lateral displacement: Challenges and perspectives. ACS nano, 14(9), pp.10784-10795.

[62] Brakke, M.K., 1951. Density gradient centrifugation: a new separation technique1. Journal of the American Chemical Society, 73(4), pp.1847-1848.

[63] Welzel, G., Seitz, D. and Schuster, S., 2015. Magnetic-activated cell sorting (MACS) can be used as a large-scale method for establishing zebrafish neuronal cell cultures. Scientific reports, 5(1), p.7959.

[64] Hu, P., Zhang, W., Xin, H. and Deng, G., 2016. Single cell isolation and analysis. Frontiers in cell and developmental biology, 4, p.116.

[65] Li, S., Ding, X., Guo, F., Chen, Y., Lapsley, M.I., Lin, S.C.S., Wang, L., McCoy, J.P., Cameron, C.E. and Huang, T.J., 2013. An on-chip, multichannel droplet sorter using standing surface acoustic waves. Analytical chemistry, 85(11), pp.5468-5474.

[66] Pan, Y., Du, X., Zhao, F. and Xu, B., 2012. Magnetic nanoparticles for the manipulation of proteins and cells. Chemical Society Reviews, 41(7), pp.2912-2942.

[67] Lapizco-Encinas, B.H., Simmons, B.A., Cummings, E.B. and Fintschenko, Y., 2004. Insulator-based dielectrophoresis for the selective concentration and separation of live bacteria in water. Electrophoresis, 25(10-11), pp.1695-1704.

[68] Buckman, C., George, T.C., Friend, S., Sutovsky, M., Miranda-Vizuete, A., Ozanon, C., Morrissey, P. and Sutovsky, P., 2009. High throughput, parallel imaging and biomarker quantification of human spermatozoa by ImageStream flow cytometry. Systems biology in reproductive medicine, 55(5-6), pp.244-251.

[69] Wang, X. and Li, S., 2014. Protein mislocalization: mechanisms, functions and clinical applications in cancer. Biochimica et Biophysica Acta (BBA)-Reviews on Cancer, 1846(1), pp.13-25.

[70] Jiao, W., Lin, H.M., Datta, J., Braunschweig, T., Chung, J.Y., Hewitt, S.M. and Rane, S.G., 2008. Aberrant nucleocytoplasmic localization of the retinoblastoma tumor suppressor protein in human cancer correlates with moderate/poor tumor differentiation. Oncogene, 27(22), pp.3156-3164.

[71] Common Cancer Types, National Cancer Institute [Online]. Available:https://www.cancer.gov/types/common-cancers

[72] Grimwade, L.F., Fuller, K.A. and Erber, W.N., 2017. Applications of imaging flow cytometry in the diagnostic assessment of acute leukaemia. Methods, 112, pp.39-45.

[73] Matozaki, S., Nakagawa, T., Kawaguchi, R., Aozaki, R., Tsutsumi, M., Murayama, T., Koizumi, T., Nishimura, R., Isobe, T. and Chihara, K., 1995. Establishment of a myeloid leukaemic cell line (SKNO-1) from a patient with t (8; 21) who acquired monosomy 17 during disease progression. British journal of haematology, 89(4), pp.805-811.

[74] Gao, L., Shao, L., Chen, B.C. and Betzig, E., 2014. 3D live fluorescence imaging of cellular dynamics using Bessel beam plane illumination microscopy. Nature protocols, 9(5), pp.1083-1101.

[75] Müllenbroich, M.C., Turrini, L., Silvestri, L., Alterini, T., Gheisari, A., Tiso, N., Vanzi, F., Sacconi, L. and Pavone, F.S., 2018. Bessel beam illumination reduces random and systematic errors in quantitative functional studies using light-sheet microscopy. Frontiers in Cellular Neuroscience, 12, p.315.

[76] Grillo, V., Harris, J., Gazzadi, G.C., Balboni, R., Mafakheri, E., Dennis, M.R., Frabboni, S., Boyd, R.W. and Karimi, E., 2016. Generation and application of bessel beams in electron microscopy. Ultramicroscopy, 166, pp.48-60.

[77] Simon, D.S., 2020. A guided tour of light beams: From lasers to optical knots. IOP Publishing.

[78] Herman, R.M. and Wiggins, T.A., 1991. Production and uses of diffractionless beams. JOSA A, 8(6), pp.932-942.

[79] "Cancer Facts and Figures 2020," Am. Cancer Soc., 2020, [Online]. Available: https://www.cancer.org/content/dam/cancer-org/research/cancer-facts-and-statistics/annual-cancer-facts-and-figures/2020/cancer-facts-and-figures-2020.pdf.

[80] Döhner, H., Weisdorf, D.J. and Bloomfield, C.D., 2015. Acute myeloid leukemia. New England Journal of Medicine, 373(12), pp.1136-1152.

[81] Sharma, A., Sharma, S., Sharma, K., Chetri, S.P., Vashishtha, A., Singh, P., Kumar, R., Rathi, B. and Agrawal, V., 2016. Algae as crucial organisms in advancing nanotechnology: a systematic review. Journal of applied phycology, 28, pp.1759-1774.

[82] Ahmadi, A., Zorofchian Moghadamtousi, S., Abubakar, S. and Zandi, K., 2015. Antiviral potential of algae polysaccharides isolated from marine sources: a review. BioMed research international, 2015.

[83] Abdel-Raouf, N., Al-Homaidan, A.A. and Ibraheem, I., 2012. Microalgae and wastewater treatment. Saudi journal of biological sciences, 19(3), pp.257-275.

[84] Rodolfi, L., Chini Zittelli, G., Bassi, N., Padovani, G., Biondi, N., Bonini, G. and Tredici, M.R., 2009. Microalgae for oil: Strain selection, induction of lipid synthesis and outdoor mass cultivation in a low-cost photobioreactor. Biotechnology and bioengineering, 102(1), pp.100-112.

[85] Metting, F.B., 1996. Biodiversity and application of microalgae. Journal of industrial microbiology, 17, pp.477-489.

[86] A. Darzins, P. Pienkoes and L. Edye, "Current Status and Potential for Algal Biofuels Production," National Renewable Energy Laboratory (NREL), T39–T2. [Online]. Available: http://task39.sites.olt.ubc.ca/files/2013/05/IEA-Task-39-Current-Status-and-Potential-of-Algal-biofuels0.pdf.

[87] Best, R.J., Lyczakowski, J.J., Abalde-Cela, S., Yu, Z., Abell, C. and Smith, A.G., 2016. Label-free analysis and sorting of microalgae and cyanobacteria in microdroplets by intrinsic chlorophyll fluorescence for the identification of fast growing strains. Analytical chemistry, 88(21), pp.10445-10451.

[88] Gour, R.S., Chawla, A., Singh, H., Chauhan, R.S. and Kant, A., 2016. Characterization and screening of native Scenedesmus sp. isolates suitable for biofuel feedstock. PloS one, 11(5), p.e0155321.

[89] Grunwald, R. and Bock, M., 2020. Needle beams: a review. Advances in Physics: X, 5(1), p.1736950.

[90] Zhao, J., Winetraub, Y., Du, L., Van Vleck, A., Ichimura, K., Huang, C., Aasi, S.Z., Sarin, K.Y. and de la Zerda, A., 2022. Flexible method for generating needle-shaped beams and its application in optical coherence tomography. Optica, 9(8), pp.859-867.